

EVOLUTION AND PERSISTENCE OF 5- μ m HOT SPOTS AT THE GALILEO PROBE ENTRY LATITUDE

J. L. Ortiz^{1,2,†,‡}, G. S. Orton^{1,†}, S. T. Stewart^{3,†} and B. M. Fisher^{1,†,*}

¹Jet Propulsion Laboratory, California Institute of Technology, Pasadena

²Instituto de Astrofísica de Andalucía, CSIC, Granada, Spain

³California Institute of Technology, Pasadena

Short title: *5- μ m hot spots*

Submit t ed to: *Journal of Geophysics] Research - Planets*

version: 11 September 1997

Figures: 11

Tables: 2

‡ Current address: Instituto de Astrofísica de Andalucía, Apdo 3004, 18080 Granada, Spain. E-mail: ortiz@iaa.es.

† Visiting astronomer at the Infrared Telescope Facility, which is operated by the University of Hawaii under contract from the National Aeronautics and Space Administration.

* NASA/NRC Resident Research Associate

ABSTRACT

We present a study on the longitudinal locations, morphology and evolution of the $5\text{-}\mu\text{m}$ hot spots at 6.5°N latitude (planetocentric), from an extensive IRTF-NSFCAM data set spanning more than 3 years, which includes the date of the Galileo Probe entry. A probabilistic analysis of the data shows that within periods of several months to even more than a year, there are 9 or 8 longitudinal areas with high likelihood of containing a $5\text{-}\mu\text{m}$ hot spot. These areas drift together with respect to System 111 at a rate which changes only slowly in time, and they are quasi-evenly-spaced, suggesting a wave feature. A spectral analysis of the radiance data reveals that planetary wavenumbers 8, 9 and 10 are predominant in the data, 10 having more spectral power in several time periods when the speed was 103.5 m/s to 102.5 m/s, while wavenumber 8 has much more power when the speed is (99.5 ± 0.5) m/s. By assuming the Galileo Probe zonal wind speed at 6.5°N is 170 m/s (Atkinson *et al.*, 1997), our drift corrections imply a westward phase speed for the proposed wave. The wavenumbers and phase speeds can be explained by a Rossby-type wave. Since Rossby waves are weakly dispersive, a change in the dominant wavenumber can also explain the small changes in drift speed, which are observed to take place simultaneously. We take advantage of this to infer properties of the vertical structure at 6.5°N .

1.- INTRODUCTION

For the last few years, Jupiter has been intensively monitored from the NASA Infrared Telescope Facility (IRTF) on Mauna Kea, Hawaii, at a variety of wavelengths which include the 5- μm window in Jupiter's spectrum. These observations, begun to monitor evolution of the atmosphere in preparation for the the P/Shoemaker-Levy 9 collision, continued as a means to support the Galileo spacecraft, both to supplement the science returned from the spacecraft remote sensing instruments and to select atmospheric features for forthcoming orbits. We have used this extensive, high-quality database to characterize the 5- μm hot spots at the latitude of the Galileo Probe entry.

Since the realization that the Galileo Probe entered a hot spot (Orton et al., 1996), it became clear that this type of feature warranted intensive study, both from the ground and from the spacecraft. Hence, we focused our attention on them, to determine new properties and to predict their positions for the purpose of pointing the spacecraft. While at first we thought, these features formed at random longitudes on the planet, a more careful inspection of the data revealed that, this was not true once an appropriate drift rate was chosen. Thus, we pursued a probabilistic approach in order to assess the chances of succeeding in observing a hot spot by sending the Galileo spacecraft pointing command sequences with the required anticipation (frequently, more than a month in advance). Our probabilistic approach has been successful as a predictive tool for targeting several hot spots during the course of the Galileo mission, which required a choice of timing roughly 8 weeks in advance and pointing 2 weeks in advance of the observations. Examples are the hot spots observed by the Near-Infrared Mapping Spectrometer (NIMS), e.g. Irwin et al. (1997) and Roos-Scrope *et al.* (1997) and by the Solid State Imaging (SSI) camera, e.g. Vasavada et al. (1997).

Ortiz et al. (1996) presented some of these probabilistic results. By comparing the observed speed of the probability pattern seen at 5 μm with the Galileo Probe wind measurements, they concluded that both the pattern and the observed speeds were consistent with a Rossby wave. In the present paper we show the data, explain the probabilistic analysis we followed and present other important aspects of the hot spots within the time frame of the Galileo mission. We also interpret the results in terms of Rossby waves and discuss their implications on vertical structure.

For the purpose of this work, we define a hot spot as a region in Jupiter's atmosphere whose equivalent brightness temperature at 4.8 μm is greater than 240 K (equivalent to $0.18 \text{ W/m}^2/\mu\text{m/ster}$) at nadir viewing. The hot spots studied here extend from the southern edge of the North Equatorial Belt (NEB) and into the Equatorial Zone (EZ). In order to avoid confusion, we forego referring to them as NEB or EZ hot spots, but refer to their locations using only the central latitude of our study (e.g. 6.5°N planetocentric).

2.- OBSERVATIONS

Most of the images used here were obtained at 4.78 μm through the narrow-band M filter or at the 4.85- μm position of the CVF filter, using the near-infrared (NIR) facility camera NSFCAM at the 3-m NASA Infrared Telescope Facility (IRTF), at the summit of Mauna Kea, Hawaii. For the narrow band M images, the plate scale used was 0.148 arcsec/pixel and $\Delta\lambda = 0.22 \mu\text{m}$ (fig.

1), whereas for the 4.85 CVF it was 0.301 arcsec/pixel and $\Delta\lambda/\lambda = 0.04$. One image is from the MIRAC2 infrared camera on the IRTF, whose resolving power is 16% at 4.8 μm , with a plate scale of 0.39 arcsec/pixel. Several of the images are from CA SPIR camera mounted on the 2.3-m telescope at Mount Stromlo, using the M filter, centered at 4.8 μm with a spectral resolution of roughly 0.5 μm and a plate scale of 0.43 arcsec/pixel. The dates covered by the data set analyzed here begin in December, 1993, and end in July, 1997. A total of 315 images have been used for the period 1995-1997 and 14 images for the period December, 1993, to August, 1994. A list of UT dates of observation corresponding to the images used here is shown in Table I.

The seeing ranged from 0.4 to 2.0 arcseconds, except for the December, 1995, images, when the use of a polypropylene screen on the primary mirror resulted in more degraded images. Most of the images, however, were obtained under subarcsecond seeing conditions. Forty-one NSFCAM images at 1.58- μm , from June 1996 to September 1996 have been separately analyzed as well. The 1.58- μm filter is centered at 1.58 μm and $\Delta\lambda/\lambda = 0.03$. The plate scale was 0.148 arcsec/pix.

Observations of early-type stars close to Jupiter were made in the IRTF Galileo support program. We have not yet cross-calibrated these against widely accepted standards, and thus rely on absolute photometric calibrations made on only a few dates. Data were absolutely calibrated against BS7525 (γ Aql.) 011 Oct. 13, 1995, and 1 J 204 (ζ Cap.), on Oct. 3, 1996. The rest of the data set for Jupiter was calibrated relative to these observations. Future work will include the cross-calibration of the nearby early standards, and it should place the radiance observations discussed below on a firmer footing.

Most of the images in the period 1995-1996 were obtained as part of the Galileo ground-based support program carried out at the IRTF, but other images were obtained in different programs (see acknowledgments).

We also used 58 raster-scanned images taken between 1985 and 1991 to perform a similar analysis as for the December 1993 to July 1997 period. The images were obtained at the IRTF using a 0.8- μm wide filter whose effective wavelength is 4.8 μm in the same way as the 7.8- μm images described by Orton et al. (1991). The spatial resolution of these early images was highly variable, from a minimum of 2 arcsec (the aperture size) to a maximum 10 arcsec or more.

3.- DATA REDUCTION

In general, the data reduction process was standard, but because of the long baseline of this data set, there were slight variations in the method. For all images, sky subtraction and interpolation over bad pixels was performed. Flatfielding was applied to some of the images. A few of the instruments, e.g. MIRAC2 and CA SPIR, seem to have a very even response across the detector. The NSFCAM detector, however, does have fine structure in its flat, which will contribute to the absolute value errors when not applied. To improve the signal to noise ratio (S/NT), in some cases, several images were coadded. Finally, some of the images were deconvolved to improve the spatial resolution (for Galileo spacecraft targeting purposes). To deconvolve our observed images (X s), we used a Bayesian technique, which searches for the ideal nondistorted image (Y) by minimizing the likelihood of X given Y is known ($P(X|Y)$), using a conjugate gradient method and assuming that

$P(X|Y)$ is a Gaussian distribution (see e.g Pina and Puetter, 1993). The point spread function we used was a Moffat function (Moffat, 1969), for which a radial profile is:

$$I(r) = I(0) (1 + (r/R_c)^2)^{-\beta} \quad (1)$$

where r is the distance from the central point, $I(r)$ is the intensity at distance r from the central point and R_c and β are two parameters that depend on the observing conditions. To conserve flux, we normalized the Moffat function so that the total intensity $2\pi \int_0^\infty I_0 (1 + (r/R_c)^2)^{-\beta} dr$ is unity. Ideally, one would fit the observed star profiles to equation (1) and obtain β and R_c for each Jovian observation. However, we could not afford the time needed to look for a close and bright star at $4.8 \mu\text{m}$ for each Jovian observation, and therefore we estimated β from the general shape of star profiles at various airmasses and various observing run and fixed it to 2. The value of R_c was more seeing-dependent and therefore we estimated it for each Jovian image by the minimum size of the resolved Jovian features. Fortunately the contrast is very high at $4.8 \mu\text{m}$, which allows a reliable estimation of R_c . One of our fully reduced, highest resolution full-disk images is shown in Fig. 2. All images were subsequently projected into a cylindrical map in System III longitude and planetocentric latitude.

During the analysis, a power law in the cosine of the emission angle, μ , limb-darkening correction was applied, whose exponent shall be referred to as the limb-darkening coefficient. We empirically derived the power law by fitting intensity measurements at the hot spots as the planet rotated and the emission angle changed accordingly. The typical limb-darkening coefficient of hot spots is very high, close to 1.3, higher than that corresponding to cooler regions, which makes hot spots difficult to distinguish from cooler areas of the planet when they are close to the limb. Since the limb-darkening effect is different for hot spots and cooler regions, using a single coefficient for the whole map is not strictly valid. As long as the spots are not close to the limb, this approximation is considered adequate. The ideal limb-darkening correction would know *a priori* whether a pixel were a hot or cold region and apply the correct coefficient. It would be possible to apply this sort of correction based on data from previous nights or observing runs, but this type of *a priori* forcing could bias our probabilistic analysis, and, therefore, we did not attempt to use hot and cold coefficients. In addition, the limb-darkening coefficient depends on the absolute intensity of the feature, which incurs even more difficulty in an accurate limb-darkening correction. Therefore, we simply preferred to restrict our analysis to points with μ higher than 0.4.

Using the photometrically calibrated images obtained on Oct. 13, 1995, and Oct. 3, 1996, the rest of the maps were relatively calibrated. The reference data were calibrated against the flux standards γ Aquila (BS 7525) and ζ Cap. (BS 8204), respectively, at close airmasses (< 0.3 difference). We did not assume that the total flux from Jupiter was constant in time at $5 \mu\text{m}$ because of concern about the effect of large, variable hot spots near the central meridian. Instead, we assumed that the belt-zone structure remained unchanged, and we applied a least squares fit to each map, weighting the equatorial intensity by a factor of 10, for the calibration factor needed to match a central meridian slice, averaged over 20 degrees in longitude. We found that the belt-zone structure changed slightly between 1995 and 1996, but that our two reference images provided a good fit to all the data.

4.- UNCERTAINTIES

The error in fitting the limb for cylindrical mapping usually yields uncertainties of ± 1 pixel in the center of the images, which translates into 0.5° to 10° uncertainty in the final maps at the disk center. The uncertainty in the plate scale and orientation of the north pole of the planet contribute as well, especially for points far from the center of the disk. For the $\mu > 0.4$ data which we included in the analysis, the uncertainty is always less than 3° , decreasing with increasing μ . In general, the S/N of the hot spots was greater than 100. We had handful of images where the S/h^T was very low, making the limb fitting process more uncertain, resulting in larger mapping errors. For those cases, we estimate uncertainties of $\pm 3^\circ$ at the center of the disk and reaching 100 close to the minimum μ value used here.

The uncertainties in our reference calibrated images is $< 15\%$. The two stars have uncertainties of $\sim 8\%$. No airmass correction was applied during the photometric calibration, possibly adding another 3%. These NSFCAM reference images were flat-fielded. When the flat-fielding was not applied, the values across the disk could be off by $\sim 5\%$. In all images except those taken before February, 1995, the standard deviation of the background was included in the error analysis. These errors were propagated through the central meridian scaling calibration. The complete data set has an average error of $\sim 20\%$ in the equatorial region. We note that the absolute calibration errors of hot spots and belts is lower than this because the signal to noise is higher, with an error of $\sim 1.5\%$. Finally, there is an error arising from our limb-darkening correction, which we estimate to be $\sim 5\%$ in our restricted range of μ , resulting in an average error of $\sim 20\%$ for these analyses.

5.- PROBABILISTIC ANALYSIS AND RESULTS

The rows within the latitude range 3.5° - 9.5° N in each cylindrical limb darkening corrected map were added to average the brightness within the area typically covered by the hot spots in the poorer-resolution data sets. For this analysis we decided to degrade the resolution to make all the data comparable, rather than selecting only the high-resolution images. The resulting one-dimensional arrays (intensity versus longitude) are referred here to as "calibrated scans".

In order to test our absolute calibration, we also generated a different set of scans, which we call "normalized scans". These scans were normalized so that the maximum value in each scan is 1. There is always at least one hot spot in each scan, which takes the intensity 1 at its hottest area. We used and compared the results from both calibrated and normalized scans.

In the scans, the hot spots were defined as a feature with an intensity higher than a so-called "threshold value". The threshold for the calibrated scans was $0.18 \text{ W/m}^2/\mu\text{m/sr}$, or 240 K. For the stall-lor[aliziatiC]- technique, the threshold was set to 0.7 for most of the investigation, unless otherwise noted. The scan can be corrected for drift with respect to System 111 by selecting a particular rotation period (corresponding to a chosen drift speed) and translating the System-III longitudes of each scan into the System-111 longitudes that the scan would have at a particular date and time. Our systems of longitude are based on different rotation periods than that of System 111, but they coincide with System 111 at a reference date, which we have taken as December 7, 1995,

at 22.1 UT (the Galileo-Probe entry date and time).

For each particular drift-corrected longitude, the probability of finding a hot spot was computed as the number of scans in which the intensity at that longitude exceeded the threshold, divided by the number of scans that covered the particular longitude. In addition, a “mean brightness” was computed as the sum of the intensity at that longitude in all the scans divided by the number of scans that contained the longitude. Therefore, this is a magnitude describing the time-averaged brightness. We determined drift speeds by looking for the speed that gave the highest probability peaks. The initial value was estimated by aligning excerpts of the maps by visual inspection, as shown in Fig. 3.

For the probability and averaged-brightness analysis we included only two images per observing date in order not to bias the analysis, because using a different number of maps per night on different nights could give unrealistic weights to some areas. We used several subsets of the data covering different periods of time, as well as a combination of all the data in the probability and averaged-brightness analysis. Using all the data from December 1993 to July 1997, there is weak indication of any preferred locations for the hot spots for any choice of the zonal drift correction value. As an example, we show (fig. 4) the probability of finding a hot spot versus longitude in a system that rotates at 103.5 m/s faster than System 111, as well as the mean intensity. The plot includes all the data from December 1993 to July 1997 and the speed used corresponds to the drift speed we measured for the Prohm-entry 5- μ m hot spot. Fig. 5 shows the same for a 99.5 m/s system.

However, using shorter time periods there are areas where the probability of finding a hot spot is high in a drift-corrected system. Since the best time-sampled period corresponds to January-September 1996, we have included the analysis of that period alone, both using calibrated scans (fig. 6a) and normalized scans (fig. 6b). The wavy pattern is more clearly seen in fig. 6b because the analysis was restricted to points with $\mu > 0.7$ for which the uncertainties discussed in section 4 are low. There are 8 peaks with mean angular separation of $\sim 45^\circ$.

Also, the January-December 1995 period is well-sampled and has been separately analyzed (fig. 7). There are 9 or 10 probability peaks, apparently one or two more than in the period January-September 1996, and the drift speed is higher than that for January-September 1996 (by 3.9 m/s).

We conclude from analyzing these data sets that the speed of the hot spot system relative to System 111 changed a maximum $\sim 4\%$ within more than three years and also that the number of peaks changed in that period of time. If the mean speed of the features changed by as little as 2 m/s, there would be a change in drift rate of $\sim 0.1^\circ/\text{day}$ or 36° after one year, which could blur most of the peaks when using data sets more than a year long. Therefore, we can see peaks only if we use data over a period less than a year long, provided that the mean speed does not change more than 1-2 m/s. If we use a very long time baseline, the peaks become blurred. This, indeed, happens when we combine the entire data set from December 1993 to July 1997. We have verified this by using 58 cylindrical maps generated from raster scanning images (see e.g. Orton et al. 1991), covering the period from 1984 to 1991. There are no clear peaks at any constant speeds in the range 80 to 120 m/s. One might think that by using a time-dependent drift speed correction, we should be able to keep track of the probability peaks. This is not the case: we find that not only

does the speed change but also the number of probability peaks, preventing a continuous track of the peaks (see sections 6 and 7).

High spatial resolution red and NIR continuum images reveal that regions of exactly the same morphology as the hot-spots $4.8 \mu\text{m}$ are very dark (see fig. 2 of Orton et al., 1996 for a comparison of a Hubble Space Telescope $9500\text{-}\text{\AA}$ image and a $4.8\text{-}\mu\text{m}$ NSFCAM image), although the converse is not true: not all the dark features seen at red and NIR filters are bright at $4.8 \mu\text{m}$. Based on the anticorrelation at 4.8- and $1.58\text{-}\mu\text{m}$ images (bright $4.8\text{-}\mu\text{m}$ areas are dark $1.58\text{-}\mu\text{m}$ areas), we used 41 of them and performed a similar analysis to that at $4.8 \mu\text{m}$, using normalized scans. In this case, the probability of a given area being bright has minima at the $5\text{-}\mu\text{m}$ hot spot sites, as we would expect based on the anticorrelation mentioned above. A total of 41 normalized scans have been used for the analysis of the period from January to September 1996, confirming the existence of the same peaks we see at $4.8 \mu\text{m}$.

The historical observations of these features in the visible recognized their prominence, and drift plots of their locations (e.g. Fig. 9.3 of Rogers 1995) show similarities to their $5\text{-}\mu\text{m}$ appearance: their quasi-periodic, but often asymmetric, spacing in longitude, as well as their time-variable number around a full circumference of the planet. Rogers (1995) also comments on the historical record of these “dark NEB projections” as often having lifetimes of months, with a faded feature reappearing in the same location. He also comments that there has been little observable in the way of general patterns or principles governing their time-dependent behavior. One exception is the fairly well-documented history of their disruption by the passage through the NEB of vigorous and turbulent active fronts marked by the appearance of white spots or streaks near the middle of the NEB, known as “rifts”. Finally, Rogers notes that the drift rate associated with features near the prograde jet at 7°N (the “North Equatorial Current”) has a velocity which is slowly varying with time and has typical values close to, although slightly above, those which we report, *i.e.* in the $103\text{-}108 \text{ m/s}$ range (see his Table 9.1).

Since red-NIR CCD observations of Jupiter are being obtained regularly by several groups and observatories, a probabilistic or a spectral analysis should give similar results to those obtained here. We encourage other groups with long-term coverage of Jupiter in the NIR to perform similar analyses.

6.- SPECTRAL ANALYSIS OF THE WAVES

Since the shape of the probability plots resembled a wave, we carried out a detailed search for periodicities in all of our scans. We generated a large file by appending all the drift-corrected scans in sets of 360 degrees in length and performed a spectral analysis of the data obtained within different time periods. Since the data are unevenly sampled in longitude we used Lomb’s periodogram (Lomb, 1976), and therefore, we obtained normalized spectral power density as a function of frequency (in cycles per degree of longitude) which we translated into planetary wavenumber (number of wavelengths in one planetary circumference). It was remarkable that we found extremely high powers for integer planetary wavenumbers, and the peaks were very sharp, clearly above the 99% significance level. As an example, we examine here the spectra of the two inter-

esting, well-sampled periods discussed in the probabilistic analysis. A detailed description of the 3-year temporal evolution is summarized in the next section, and in table 11.

For the period January-September 1996 using the 99.6 m/s speed we found that there were two main periodicities: one at wavenumber 8 and a much weaker one at 9 (fig 8). For the period January-December 1995, using the 103.5 m/s speed we found a clear periodicity at wavenumber 10 (fig. 9). This could mean that the waves are slightly dispersive, something that is confirmed in the temporal evolution section below.

Since the waves move at about 7.1 degrees/day, they complete a circumference in $360/7.1 \simeq 50$ days. Therefore, we do not expect to see a very large change in the spectral power of any given wavenumber within time periods much shorter than 25 days. Thus, we performed the time evolution analysis in two-month time steps.

7.- SPEED AS A FUNCTION OF TIME WITHIN 6-MONTH INTERVALS

The speed of the waves can be finely tuned by selecting the speed that gives the frequency closest to 8, 9 or 10 wavenumber, and the highest spectral power. We can therefore obtain the drift speed as a function of time. We usually obtained integer wavenumbers with a precision of ± 0.01 when using ~ 20 scans and ± 0.001 when using sets of ~ 100 scans. The drift estimations made this way were usually very close to those obtained by looking for the speed that gave the highest probability peaks. We used 13 data sets of six-month intervals shifted by two months.

The derived drift speeds are therefore representative of the middle or the last days of the periods. Table 11 lists the different wave speeds and wavenumbers with their spectral power as a function of 2 month intervals.

When there are wavenumbers of comparable power, the "mean speed" is not easily found. As a general trend, using speeds closer to 102.5 m/s, the spectral power of wavenumber 10 increases, whereas using 100.5 m/s or 99.5 m/s the spectral power of wavenumber 8 increases. There are a few cases in which one of the wave modes overwhelms the others (last rows on table 11). For those cases the speeds 99.5 m/s for wavenumber 8 and 102.5 m/s for wavenumber 10, gave the highest spectral power. That is consistent with slightly dispersive waves, which travel at slightly different velocities, depending on the wavenumber. Thus, by picking the right velocity for a wavenumber, its spectral power increases, whereas another periodic feature with different wavenumber is somewhat blurred by using a speed that is slightly off, causing a decrease in spectral power.

As seen in Table 11, the planetary wavenumber we observed the most was 8, corresponding to a mean speed close to 99.5 m/s. As shown in the table, changes in the dominant wavenumbers took place on several occasions.

In the period December 1993 to August 1994, for which we do not have enough data to do a 2-month by 2-month analysis, the spectral power shows a peak at planetary wavenumber 8 and a smaller one at wavenumber 15, using a drift rate of 101.5 m/s. Speeds lower than that by just 0.3 m/s result in a loss of spectral power. Using a higher speed, e.g. 102.5 m/s, the maximum power

is less than that at 101.5 m/s and takes place at wavenumber 8 as well. There is a smaller peak at 15 that increases in spectral power as we approach 104.5 m/s where it reaches its maximum. This is, again, consistent with the dispersive properties already discussed. The low number of images we have for this period (only 14) does not allow us to compute very accurate drift rates based on the probabilistic approach, but we can estimate that the highest probabilistic peaks are obtained between 101.5 m/s and 100.5 m/s.

Concerning the raster scan data, from 1985 to 1991, we have less than 13 maps per year, on average, they are of low spatial resolution, the navigation is worse and, thus, we might expect much less conclusive results. Arranging the data in groups of maps close in time, the data from August 1985 to October 1985 show a peak at wavenumber 7 for 14 maps and 102.5 m/s, although it is below the 99% significance level. The data from June 1987 to January 1988 show a peak at wavenumber 4, for 13 scans at 100.5 m/s, although it is below the 99% significance level. The data from October 1988 to March 1989 show nothing conclusive (12 scans) and the data from September 1989 to May 1990 show nothing conclusive (9 scans).

Just prior to the compilation of these results we became aware of work by Harrington et al. (1996) who searched for waves in the 5- μ m window using mosaics of PROTOCAM images taken in 1992. Their search for waves began by searching for periodicities in individual cylindrical maps (with full longitudinal coverage), averaging of spectral power followed by a sinusoidal fit to the wavenumber of maximum averaged spectral power and a subsequent search for the speed which accounts for the different phases they were obtaining in different nights. This approach is basically equivalent to ours, although we shifted the scans in advance and did not carry out any averaging. Their results for the latitude we are concerned show a wave of wavenumber 10, and a speed of $104.5 \text{ m/s} \pm 0.5 \text{ m/s}$, for the first half of 1992. As they used only 19 maps and possibly because of their averaging technique to compute power spectra, they did not find several propagating modes with different wavenumbers as we did. Their speed is very close to the 103.5 m/s derived by us for epochs when the wavenumber was predominantly 10. Other coincidences with Harrington et al. (1996) are that they used a similar approach to correct their maps for limb darkening. They used a μ^{d-1} dependence, with $d=2.25$, while our d would have been 2.30. They report not using data 45 degrees away from the central meridian (which is close to our μ cutoff) and therefore their data analysis was similar to ours, although their database was more limited in time and spatial resolution.

8.- MORPHOLOGY AND LIFETIME OF HOT SPOTS

As shown in a movie presented by Stewart and Orton (1997), and summarized in Orton et al. (1997), the Probe Entry Site (PES) hot spot evolved in a complex fashion, it sometimes got dimmer, it brightened and it even became double (or in other words, it split) somewhat erratically. Nevertheless there seemed to be a trend of increasing brightness after September 1995, that peaked a few weeks after the probe entry (Orton et al., 1997).

The evolution of the brightness temperature of another hot spot as a function of time is depicted in fig. 10. For this plot, the brightness has been averaged over a region 8° by 6° in longitude and latitude respectively, around the hot spot longitude-shifted location. Points with μ smaller than 0.7 were rejected. The speed was varied as a function of time in order to keep the spot centered.

We used 103.5 m/s for the period March 1995 to December 1995, 100 m/s from January 1996 to May 1996, and 99.5 m/s from June 1996 to July 1997. Error bars are 20% of the radiance,

As can be seen, the hot spot brightness reached its maximum about ~ 300 days after we started tracking it, around 252 K, although the core of the hot spot must have reached a higher temperature, as we are plotting averages within an area 8° by 6° wide.

The highest peak temperature we have ever recorded in all the observed hot spots was 276 K, but NIMS has recorded even higher temperatures (Carlson et al. 1996, Roos-Serote et al., 1997) most likely as a result of the higher resolution obtainable with NIMS and possibly because of different absolute calibrations. From the statistics of the 315 images analyzed here, the mean latitude where the maxima are reached is 7.3° with a standard deviation of 0.9° . The averaged maximum brightness is $0.39 \text{ W/m}^2/\mu\text{m/sr}$ with a standard deviation of $0.11 \text{ W/m}^2/\mu\text{m/sr}$. Although it is highly unlikely, our algorithm for detection and interpolation over bad pixels may have contributed to lower our peak temperatures.

Concerning the evolution of other hot spots, we could see a variety of behaviors. On some occasions, we can even see two separate hot spots approach one another and possibly merge. The number of hot spots is almost always higher than 10 or 11, whereas our number of probability peaks is less than those figures. In that sense, the number of areas where the probability of finding a hot spot is high seems to represent the higher power wavenumber of our proposed wave, and therefore the wavenumber does not coincide with the actual number of hot spots. At least part of the merging and splitting phenomena could be the result of interaction (*or* birth) of different wave modes (wavenumbers) which move at slightly different speeds. Some of the hot spots may “belong to a wave” and some others belong to a different one with a different, wavenumber. Sometimes a set of evenly separated hot spots seems to encircle a full hemisphere of the planet, while another set of hot spots are closer together in the other hemisphere and thus represent a wave of higher wavenumber in that hemisphere. This could also explain the fact that some hot spots seem to move a little faster than others, when we track them individually.

Although the morphology evolution is complex, most of the hot spots seem to show a “mature” phase in which they are large (several degrees wide in longitude and about 3 degrees in latitude), with a hot narrow festoon extending south and westward from the easternmost edge, tilted about 30° , much like the hot spot captured by NIMS or the SS1 during the fourth (Europa-4, or N-4) orbit encounter (see, for example, Roos-Serote et al. 1997, or Vasavada et al. 1997). At this mature stage they also have tail-like feature extending northward of the northwest edge (fig. 2).

9.- TOTAL AREA COVERED BY HOT SPOTS

Orton et al. (1996) estimated that the total area covered by $5\text{-}\mu\text{m}$ hot spots was $< 1\%$ of the planet. For the hot spot definition here (brightness temperature higher than 240 K) more detailed calculations show that about 98 to 328 squared degrees are occupied by the 7.3° hot spots, depending on the maps we use and on the limb-darkening coefficient we apply. This represents 0.1 to 0.5% of the area of Jupiter (fig. 11).

10.- DISCUSSION

The large areas that we track from the ground could be the result of an organized circulation pattern. Vasavada et al. (1997) have tracked clouds moving northeast toward a hot spot using SS1 images. They infer an anti-cyclonic vortex between the equator and NEB. Based on Voyager and Hubble Space Telescope images, Beebe (1997) has previously proposed a series of such vortices surrounding the equatorial region which could account for the nearly evenly spaced nature of hot spots. The clearing of the clouds which is associated with hot spots may be the result of shearing between the vortices and NEB, although no observations to date have tracked clouds fully around these proposed vortices.

Rosby waves could be the organized circulation that we observed because visual and thermal features can be expected to trace the oscillations of some combination of the temperature, the geopotential and the vertical motion fields associated to the waves. In the past, wave propagation has also been suggested (Smith et al., 1979, Mitchell et al. 1979, Huut et al., 1981) to explain the 11-13 plumes observed during Voyager encounters. If we adopt 160 m/s as the mean jet speed (\bar{u}), just 10 m/s less than that measured by the Galileo probe (Atkinson et al., 1997), but still within their errors, the Rossby wave would move at 103- 160 \simeq - 57 m/s. As seen in table II, the high-spectral-power planetary wavenumber was 10 at the time of probe entry.

In order for Rossby waves to account for a phase speed (relative to the mean zonal wind) of -57 m/s ($c - \bar{u} \simeq -57$ m/s) and a wavenumber = 10, using the dispersion relation of a midlatitude Rossby wave as found in e.g. Gill (1982) we have:

$$c - \bar{u} = - \frac{\beta}{k^2 + l^2 + m^2 f^2 / N^2} \quad (2)$$

then, $l^2 + m^2 f^2 / N^2 = 5.94 \cdot 10^{-14} \text{ m}^{-2}$.

In (2), c is the wave phase speed, \bar{u} is the mean zonal wind, $\beta = df/d\lambda$, f is the Coriolis parameter, N the buoyancy frequency and k, l, m are the zonal, meridional and vertical wavenumbers respectively. Using $l^2 + m^2 f^2 / N^2$ derived from the dispersion relation and changing the wavenumber from 10 to 8 we obtain an increase of ~ 5 m/s in the westward speed, which is very close to the observed increase of ~ 4 m/s in our data. The result would be 7 m/s if we used 180 m/s as the mean jet speed. The changes in the drift-correction we needed to apply to our scan could also be due to changes in the jet speed. The jet speeds are currently thought to have been the same for many years, but changes of only a few m/s are difficult to rule out. Regarding l and m , if we assume that the contribution of the vertical wave is small, then, the meridional wavelength should be about 4000 km. If we assume that the contribution of l is small (the meridional wavelength is large), the vertical stratospheric wavelength would be about 80 km (for the value of N used here, 10^{-2} s^{-1}), or a few Jovian scale heights, consistent with the larger component of the temperature oscillations seen at equatorial latitudes by Lindal et al. (1981).

Although the dispersion relation strictly applies to midlatitudes, it should not be far from the behavior we would expect at 6.5° where the Rossby number is not as small as in midlatitudes. A more sophisticated study of Jovian equatorial waves, based on linear perturbation of the momentum,

cent inuity and energy equations was carried out by Allison (1990), although he neglected shear, forcing and dissipation. Allison presented a model of Jovian equatorial waves with discussion of their possible dispersion properties and vertical structure, applied to the 11 - 13 equatorial plumes seen by Voyager (Smith et al., 1979), which he argued could represent a Rossby wave of planetary wavenumber 11 -13. No "active" plumes were observed during the time period discussed here, but the active plumes seen by Voyager were always next to dark-continuum features, which are the hot spots seen at $5 \mu\text{m}$. Although we do not think the number of plumes or the number of hot spots represent the actual wavenumbers, the treatment by Allison (1990) applies to the wave phenomena in general, not necessarily to the plumes. Using Allison's dispersion relation for Rossby equatorial waves, the -57 m/s of our proposed wave is matched with wavenumber 10, meridional index $j=1$ and using an equivalent depth (h) of 2.2 km, which translates into a vertical stratospheric wavelength of a few Jovian scale heights, depending on the exact value of the static stability parameter. This is very close to our analysis of midlatitude Rossby waves, and this is compatible with at least part of the oscillations seen in the vertical pressure-temperature (P-T) profiles at equatorial latitudes from Voyager by Lindal et al. (1988). Latitudinal trapping of Rossby waves at the latitude of the probe entry is very effective for the equivalent depth suggested here, as can be seen in fig. 4 of Allison (1990). The temporal change in phase speed is also accounted for by using a change in wavenumber 8 to 10. For $h=2.2 \text{ km}$, the change of speed would be 5 m/s , just 1 m/s more than the $\sim 4 \text{ m/s}$ change observed. If the zonal jet speed were 180 m/s instead of 160 m/s , the required equivalent depth would be 4.5 km , still within the range of plausible values. According to Allison's growth rates for waves with different wavenumbers, the growth rate for a $k=9$ Rossby Wave maximizes at an equivalent depth of about 4 km . However, for these values of h , the change in speed associated to a change of wavenumber 10 to 8 would be 10 m/s , a factor of 2 more than observed. Since the vertical structure is coupled to the value of h , it is likely that h itself has a strong longitudinal dependence, because the vertical structure is obviously not the same at plumes and hot spots. This could argue for several wavenumbers present, not only one, and indeed this is observed in our analysis.

Another interesting characteristic of Rossby waves is that the vertical motion field of the wave (w) could be such that w is less than zero at the hot spots and higher than zero at the plumes, which could explain the hypothesized deep downdrafts at hot spots and updrafts at plumes. Since plumes are always between hot spots, they could possibly be 180 degrees out of phase with respect to the hot spots. The magnitude of the downward velocity, can only be determined by solving the entire set of perturbed momentum, continuity and energy equations, but since the magnitude of the perturbation of some of the meteorologic variables seems to be of the same order of the averages, by linearizing the perturbed equations we only get a crude approximation to the actual problem. A more complete study would require solving the nonlinear perturbed equations, including shear, forcing and dissipation.

Very recently, Deming et al. (1997) have also claimed the need for Rossby waves to justify their thermal infrared propagating features. The structure seen in their $7-13 \mu\text{m}$ channel (which is influenced both by temperature and cloud fields) moves with approximately $130 (\pm) 26 \text{ m/s}$. It is worth noting that their spatial power spectra has a maximum at wavenumber 7 - 8 although they have components in the interval 1 to 10 wavenumbers.

Fisher *et al.* (1997) have shown power spectra of their retrieved tropospheric temperatures, with

important components with wavenumbers 1-10, which propagate very slowly with respect to System 11 I. A much simpler analysis of this question was addressed by Orton et al. (1994) for similar data, who found the temperature waves to be moving slowly. These results persist up to temperatures near the 250-mbar level and higher, where the influence of cloud opacity was low and any zonal periodicity in the cloud structure is unlikely to impose itself on the temperature field. A comparison of the 5- μm hot spot locations and the locations of peaks or troughs of waves in the tropospheric temperature field shows no correlation at all (Orton et al., 1997).

One can wonder whether we could see wave-like phenomena of the same type at comparable latitudes in the southern hemisphere. Considering that the jet speed and even the vertical structure are different, we do not necessarily expect to see these same phenomena. Nevertheless, in the nineteenth century, the SEBn was highly disturbed, and the NEBs was quiet. According to Rogers (1995), who compiled drawings of Jupiter from historical records, the SEBn features were much like the ones we observe on the NEBs today. The only notable difference from today's NEBs features was the spacing, which might imply a different wavenumber in these features.

11.- IMPLICATIONS FOR THE VERTICAL STRUCTURE

From the analysis above, we derive an upper limit for the equivalent depth (h) of about 4 km and a lower limit of 2.2 km, using the most updated speed of the deep zonal winds measured by the probe (Atkinson et al. 1997), although values of h closer to 2 km are favored by the slightly dispersive properties of the wave phenomena that we found. Using a four layer vertical structure as proposed by Allison (1990), a stratospheric layer (A) with large stability, a slightly stable tropospheric layer (B), a clearly subadiabatic layer (C) and a purely adiabatic layer (D), we can gain some insight on the real Jovian atmosphere. If we assume that h is 4 km, there must be a layer B with $\Gamma/g \ll 1$ km (where Γ is the static stability parameter), which means that there is a very slightly subadiabatic region or the vertically propagating wave would not exist. The vertical temperature profiles obtained by Lindal et al. (1981) show that there could be a layer matching these characteristics, located at the levels of the ammonia cloud, that is, at about 300-700 mbar. The zonal propagation of a Rossby wave requires the presence of a stable layer or duct layer (which we denominate C) where the wave is trapped. Although most of the investigators have proposed that the stable layer is a water cloud layer, where the latent heat release is causing the subadiabatic profile needed, there might be other possibilities for stabilization, such as radiative processes. A stable layer is observed in the P-T profile by the atmospheric structure instrument of the Galileo probe (Stiff et al., 1996). It extends from at least 5 to 14 bars. We do not know the thickness of this layer, but it is at least 2 or 3 scale heights. Calculating the static stability Γ/g from the P-T profile by Seiff et al., we get 6.5 km and using $h=4$ km together with equation 22 of Allison (1990) we derive a thickness for the stable layer of 0.8 scale heights. This is about a factor of 2 too small, but we must recall that equation 22 of Allison holds only for combined thickness of the B and C layer much larger than the thickness of Layer C, which is not the case. A deeper, fully adiabatic fourth layer (D) would be required as well. Although we do not have any observational evidence of it, convection is thought to be the only means of heat transport deep in the atmosphere and therefore, we expect an adiabatic profile there.

Other constraints on the cloud structure obtained from our study are related to the center-to-limb behavior of the 5- μm outgoing radiance. The fact that the limb darkening is higher for the hot spots

than for the rest of the planet and its exact value can tell us something about the cloud structure, but this needs detailed radiative transfer modeling which we defer to future work. All hot spot radiative transfer models should fit this constraint of having a strong limb darkening coefficient, close to 1.3, with higher temperatures having higher coefficients.

12.- CONCLUSIONS

Within periods of several months to a year, there are quasi-evenly-separated regions that move with speed ~ 100 m/s with respect to System 111 and where the probability of finding a hot spot is considerably higher than in their surroundings. The time-averaged $5\text{-}\mu\text{m}$ brightness has peaks there as well. This speed changed slightly as function of time (a maximum 4 % in three years). These oscillating patterns of probability resemble a wave and motivated a detailed spectral study of propagating features in our data set, which reveals that wavenumbers 8, 9 and 10 are present most of the time in the data, with different spectral powers in different dates.

Rossby waves can explain the speed of these features compared to the *in situ* zonal wind measurements made by the Galileo Probe at a time covered by our data (Atkinson et al., 1997). They can also explain the observed wavenumbers and the change of speed with time can be interpreted as changes in the predominant power of wavenumbers 8, 9, 10, which can lead to a change of the westward Rossby phase speed, because of the dispersive nature of Rossby waves. Hot spots are well-described as a superposition of a few Rossby waves of several wavenumbers traveling along the planet at slightly different speeds, depending on the wavenumber. This can explain most of the phenomenology seen when tracking single hot spots, although the mechanism which power different wavenumbers are not yet conclusively identified. Their slightly dispersive properties give us information on the Jovian vertical structure which is compatible with the atmospheric structure measurements by the Galileo Probe (Seiff et al., 1996).

ACKNOWLEDGMENTS

A. J. Friedson is acknowledged for very useful discussions on planetary waves. We are grateful to the many people who contributed to obtaining the data, either by observing or by sharing part of their valuable observing time. We are also grateful to some other scientists and students for their help in many subjects. Thanks go to: K. Baines, C. Connor, C. Dumas, W. Golisch, D. Griep, R. Joseph, C. Kaminski, M. Marinova, P. Martin, M. Ressler, J. Spencer, J. Spitale, J. Stansberry, P. Yanamandra-Fisher, and the NASA IRTF staff.

REFERENCES

- Allison M., 1990. Planetary Waves in Jupiter's Equatorial Atmosphere. *Icarus*, 83, 282-307.
- Atkinson, D. H., A. P. Ingersoll and A. Stiff 1997. Deep winds on Jupiter measured by the Galileo Probe. *Nature*, 388, 649-650.
- Beebe, R. F. 1997. Personal communication.
- Carlson, R., W. Smythe, K. Baines, E. Barbinis, K. Becker, R. Burns, S. Calcutt, W. Calvin, R. Clark, G. Danielson, A. Davies, P. Drossart, T. Encrenaz, F. Fanale, J. Granahan, G. Hansen, P. Herrera, C. Hibbitts, J. Hui, I. Irwin, T. Johnson, L. Kamp, H. Kieffer, F. Leader, E. Lellouch, R. Lopes-Gueiter, D. Matson, T. McCord, R. Mehlman, A. Ocampo, G. Orton, M. Roos-Serote, M. Segura, J. Shirley, L. Soderblom, A. Stevenson, J. Torson, F. Taylor, A. Weir, and P. Weissman. 1996. Near-infrared spectroscopy and spectral mapping of Jupiter and the Galilean satellites: First results from Galileo's initial orbit. *Science* 274, 385-388.
- Carlson R. and the Galileo NIMS team 1996b. Some first results from the Near Infrared Mapping Spectrometer at Jupiter. *Bull Amer Astron Soc* 28, 1135.
- Deming D., D. Reuter, D. Jennings, G. Bjoraker, G. McCabe, K. Fast and G. Wiedemann. Observations and Analysis of Longitudinal Thermal Waves on Jupiter, 1997. *Icarus* 126, 301-312
- Fisher B. M., G. Orton, M. Ressler and S. Hinkley 1997. Jovian tropospheric horizontal and vertical temperature structure during the Galileo G 1 orbit. *Bull. Amer. Astron. Soc.* 29, 1007.
- Gill, A. E. 1982. Atmosphere-Ocean Dynamics. Academic Press Inc.
- Harrington J., T. E. Dowling and R. L. Baron, 1996. Jupiter's tropospheric thermal emission. I. Observations and techniques. *Icarus* 124, 22-31.
- Harrington J., T. E. Dowling and R. L. Baron, 1996b. Jupiter's tropospheric thermal emission. II. Power spectrum analysis and wave search. *Icarus* 124, 32-44.
- Hunt, G. E., B. J. Conrath, and J. A. Pirraglia 1981. Visible and infrared observations of the Jovian plumes during the Voyager encounter. *J. Geophys. Res.* 86, 8777-8781.
- Irwin, P. G. J., A. I. Weir, S. Smith, F. W. Taylor, A. L. Lambert, B. S. Calcutt, R. W. Carlson, K. Baines, P. Drossart, Th. Encrenaz, M. Roos-Serote. Cloud structure and atmospheric composition of Jupiter retrieved from Galileo NIMS real-time spectra. *J. Geophys. Res.* 1997 (this issue).
- Lindal, G. F., G. E. Wood, G. S. Levy, J. D. Anderson, D. N. Sweetnam, H. B. Hotz, B. J. Buckles, D. P. Holmes, P. E. Doms, V. R. Eshleman, G. L. Tyler, and T. A. Croft 1981. The atmosphere of Jupiter: An analysis of the Voyager radio occultation measurements. *J. Geophys. Res.* 86, 8721-8727.

- Lomb, N. R. 1976. *Astrophysics and Space Science*, 39, 447-462.
- Mitchell, J. L., R. J. Terrile, B. A. Smith, J-P. Mueller, A. P. Ingersoll, G. E. Hunt, S. A. Collins and R. F. Beebe. Jovian cloud structure and velocity fields. *Nature* **280**, 776-778.
- Moffat, A. F. J. (1969). A theoretical investigation of focal stellar images in the photographic emulsion an application to photographic photometry. *Astron. Astrophys.* 3, 455.
- Ortiz, J. L., G. Orton, A. J. Friedson 1996. Hot spots on Jupiter from 1994 to 1995. *Bull. Amer. Astron. Soc.* 28, 1142.
- Orton, G. S., A. J. Friedson, J. Caldwell, H. B. Hammel, K. H. Baines, J. T. Bergstralh, T. Z. Martin, M. F. Malcom, R. A. West, W. F. Golisch, D. M. Griep, C. D. Kaminski, A. T. Tokunaga, R. Baron and M. Shure 1991. Thermal maps of Jupiter: Spatial organization and time dependence of stratospheric temperatures, 1980 to 1990. *Science*, 252, 537-542.
- Orton, G., J. L. Ortiz, K. Baines, G. Bjoraker, U. Carsenty, F. Colas, D. Deming, P. Drossart, E. Frappa, J. Friedson, J. Goguen, W. Golisch, D. Griep, C. Hernandez, W. Hoffmann, D. Jennings, C. Kaminski, J. Kuhn, P. Laques, S. Limaye, H. Lin, J. Lecacheux, T. Martin, G. McCabe, T. Momary, D. Parker, R. Puetter, M. Ressler, G. Reyes, P. Sada, J. Spencer, J. Spitalo, S. Stewart, J. Varsik, J. Warell, W. Wild, P. Yanamandra-Fisher, A. Dayal, L. Deutsch, G. Fazio, and J. Hera. 1996. Preliminary Results of Earth-Based Observations of the Galileo Probe Entry Site. *Science* 272, 839-840.
- Orton, G. S., S. T. Stewart, B. M. Fisher, J. L. Ortiz 1997. Characteristics of the Galileo Probe Entry Site from Earth-Based Remote Sensing Observations. *Submitted to J. Geophys. Res.*
- Pills, R. K. and Puetter, R. C. 1993. Bayesian image reconstruction: the pixon and optimal image modeling. *PASP*, 105, 630.
- Roos-Scrote, M., P. Drossart, Th. Encrenaz, F. Lellouch, R. W. Carlson, K. H. Baines, L. Kamp, R. Mehlman. Analysis of Jupiter NEB hot spots in the 4-5 μm range from Galileo/NIMS observations; measurements of water, ammonia and cloud opacity. *Submitted to J. Geophys. Res.*
- Rogers, J. H. 1995. The giant planet Jupiter. Cambridge University Press.
- Stief, A., D. B. Kirk, T. C. D. Knight, J. D. Mihaloy, R. C. Blanchard, R. E. Young, G. Schubert, U. Von Zahn, G. Lehmacher, F. S. Milos, and J. Wang. Structure of the Atmosphere of Jupiter: Galileo Probe Measurements 1996. *Science*, 272, 844-845.
- Smith, B. A., L. A. Soderblom, P. V. Johnson, A. P. Ingersoll, S. A. Collins, E. M. Shoemaker, G. E. Hunt, H. Masursky, M. H. Carr, M. A. Davis, A. F. Cook 11, J. Boyce, G. E. Danielson, T. Owen, C. Sagan, R. F. Beebe, J. Veverka, R. G. Strom, J. F. McCauley, J. Morrison, G. A. Briggs and V. E. Suomi 1979a. The Jupiter system through the eyes of Voyager I. *Science* 204, 951-972.

- Smith, B. A., L. A. Soderblom, R. Beebe, J. Boyce, G. Briggs, M. Carr, S. A. Collins, A. F. Cook II, G. E. Danielson, M. E. Davis, G. E. Hunt, A. Ingersoll, T. V. Johnson, H. Masursky, J. McCauley, D. Morrison, T. Owen, C. Sagan, E. M. Shoemaker, R. Strom, V. F. Suomi, and J. Veverka 1979b. The Galilean satellites and Jupiter: Voyager 2 imaging science results. *Science* 206, 927-950.
- Stewart, S. T., G. Orton 1997. The cloud structure and morphology of Jovian equatorial hot spots. *Bull. Amer. Astron. Soc.* 29, 1006.
- Vasavada, A. R., A. P. Ingersoll, D. Banfield, M. Bell, P. J. Gierasch, and M. J. S. Belton 1997. Galileo imaging of Jupiter's atmosphere: The Great Red Spot, equatorial region, and White ovals. *Submitted to Icarus*.

FIGURE CAPTIONS

Fig. 1. Narrow-band M filter transmission superimposed to a Voyager IRIS spectrum of a typical Jovian belt.

Fig. 2. A typical fully-reduced high resolution narrow band M image of Jupiter obtained on September 6, 1996, at 7:48:24 UT. The image is shown in false color and has been stretched logarithmically.

Fig. 3. Drift and limb-darkening corrected cylindrical maps at 13.5° to -0.5° for the dates labeled. The drift correction applied is 103.5 m/s. As can be seen, bright features align quite well in the vertical, meaning that the drift rate is a good estimate, which can be refined by the probabilistic analysis discussed in the text.

Fig. 4. Probability of finding a hot spot in the period December 1993 to July 1997 vs. longitude in a system that rotates at 103.5 m/s respect to System 111, System 111 longitudes and this system's longitudes coincide for the date of Galileo Probe Entry (December 7th, 1995 at 22.1 UT). Also plotted is the mean $4.8\text{-}\mu\text{m}$ brightness vs longitude.

Fig. 5. The same as fig. 4, using 99.6 m/s.

Fig. 6. (a) Upper graph: Probability of finding a hot spot in the period January 1996 to September 1996 vs longitude in a system that rotates at 99.6 m/s respect to System III, using calibrated scans. Lower graph: Mean radiance as a function of longitude in the same system, using calibrated scans. (b) Same as (a) using normalized scans.

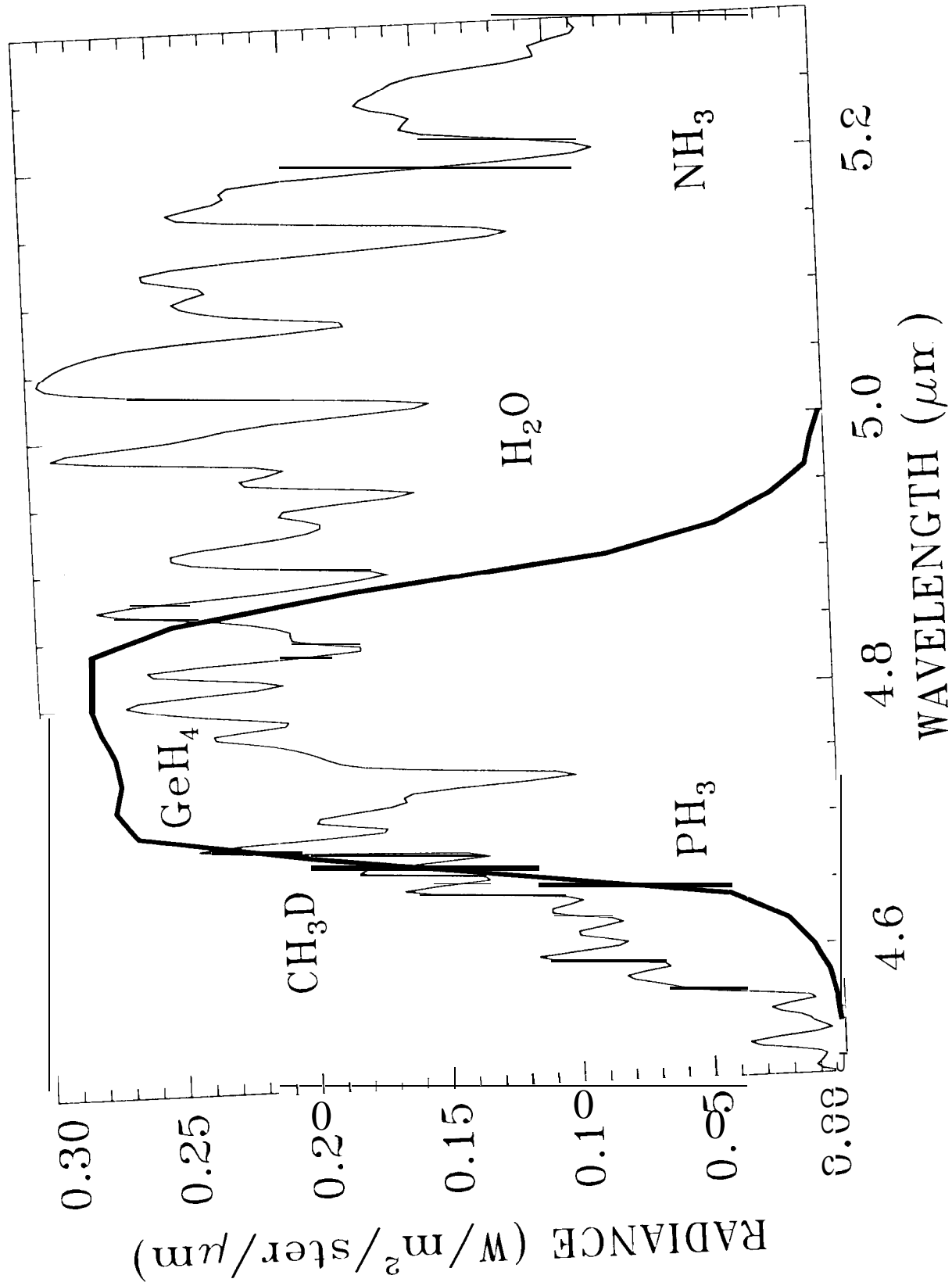
Fig. 7. Probability of finding a hot spot in the period January 1995 to December 1995 vs longitude in a system that rotates at 103.5 m/s respect to System 111.

Fig. 8. Lomb-normalized power spectral density as a function of planetary wavenumber (cycles per planetary circumference) for the $4.8\text{-}\mu\text{m}$ radiances observed in the period January to September 1996. The speed of the wave was fixed to 99.6 m/s based on the probabilistic analysis discussed on the text.

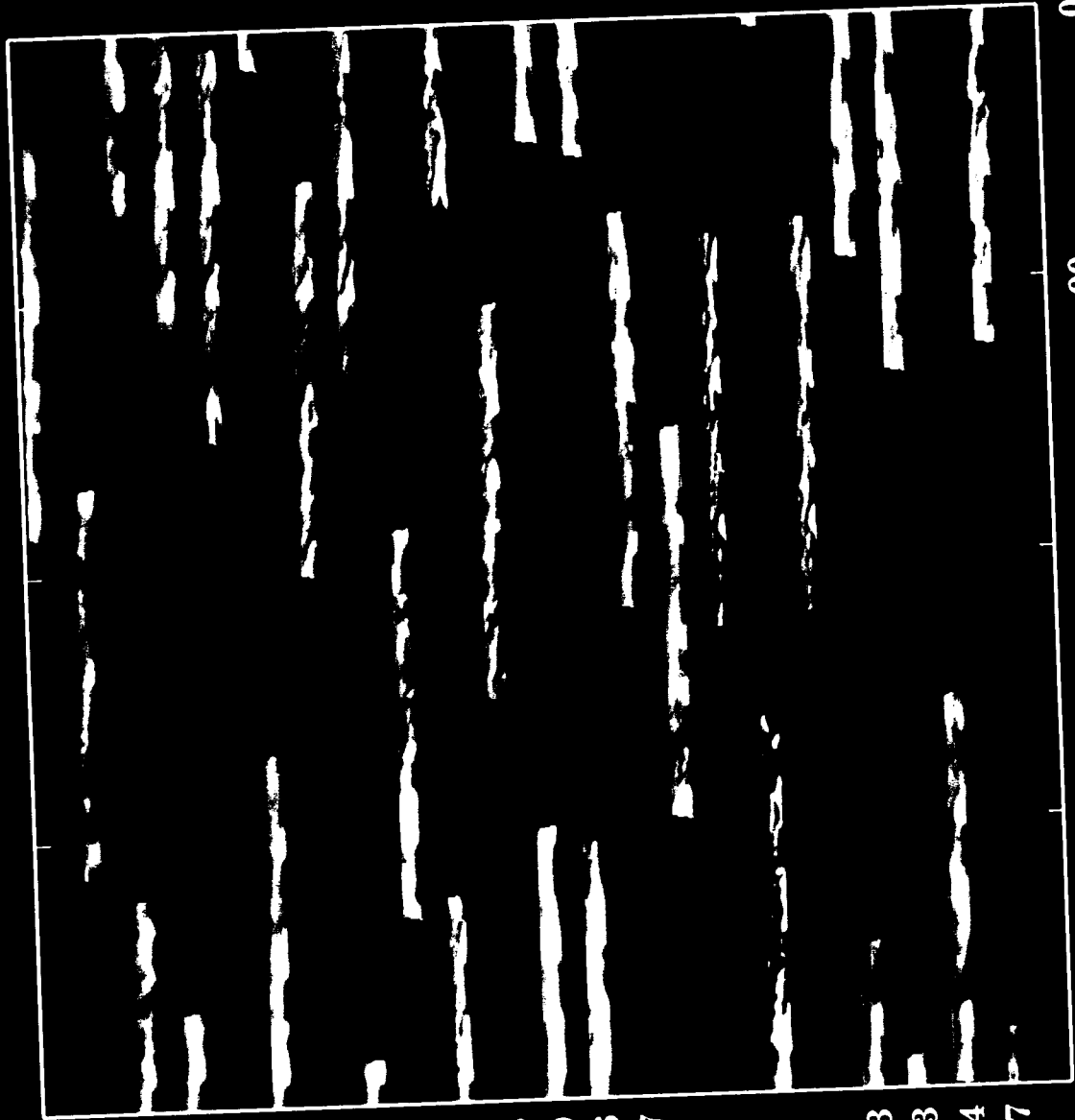
Fig. 9. Same as fig. 8 for the period January to December 1995. The speed of the wave was fixed to 103.5 m/s based on the probabilistic analysis discussed on the text.

Fig. 10. $4.8\text{-}\mu\text{m}$ radiance of a hot spot as a function of time (days) since January 1, 1995. The intensity has been averaged with a region 8° by 6° in longitude and latitude respectively centered at a System III longitude of 175° at the date of Galileo Probe entry, almost in the opposite part of the planet respect to the probe entry site hot spot.

Fig. 1). Global map at $4.8\text{ }\mu\text{m}$ on October 3, 1996. This map has been assembled from several individual images, and limb-darkening has been corrected using a limb-darkening coefficient $k=1.2$, which is good for hot spots only, and overestimates the correction for other features. The total projected area containing hot spots (brightness temperature higher than 24(I K) is 65 to 235 degrees², or 0.1 to 0.5% of the map.

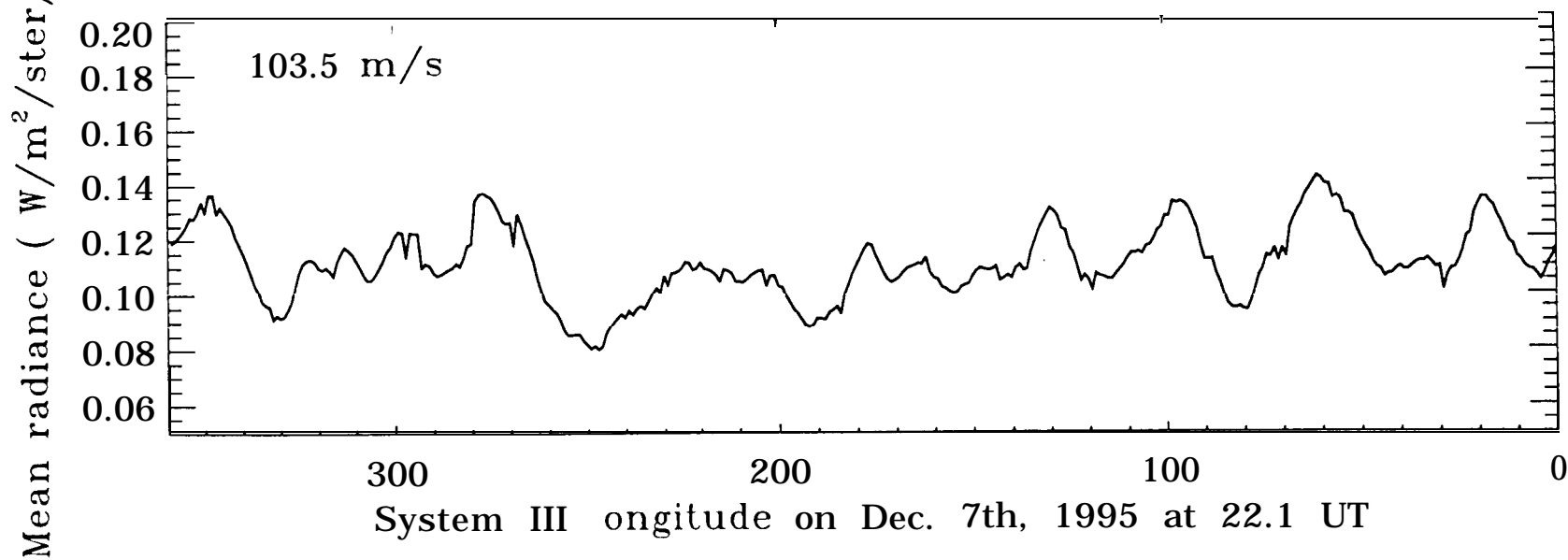
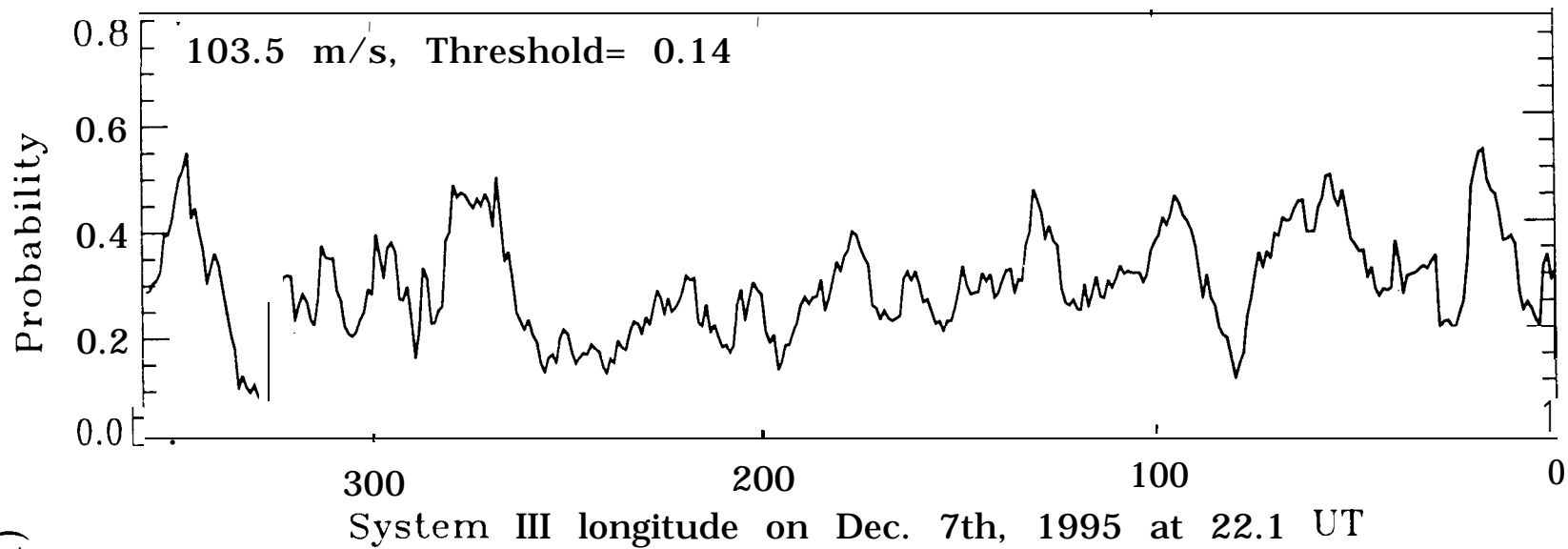


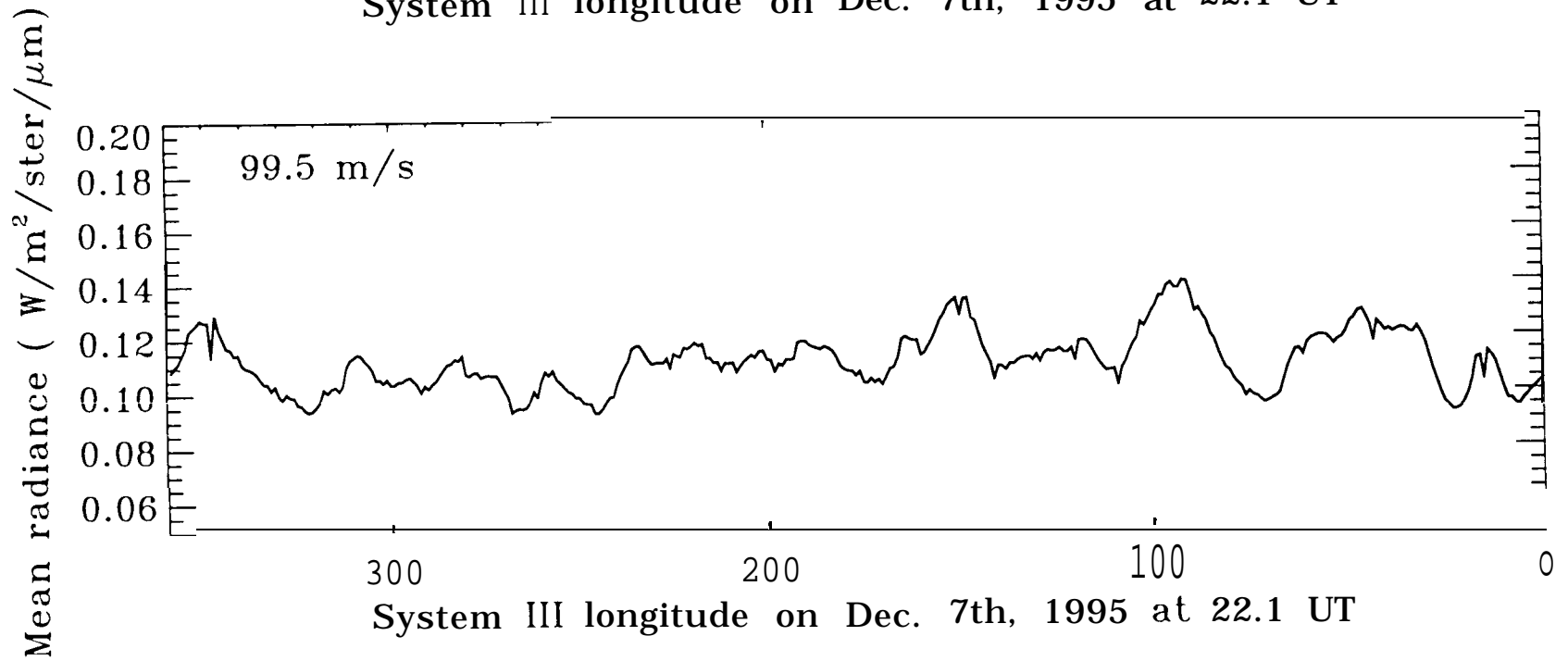
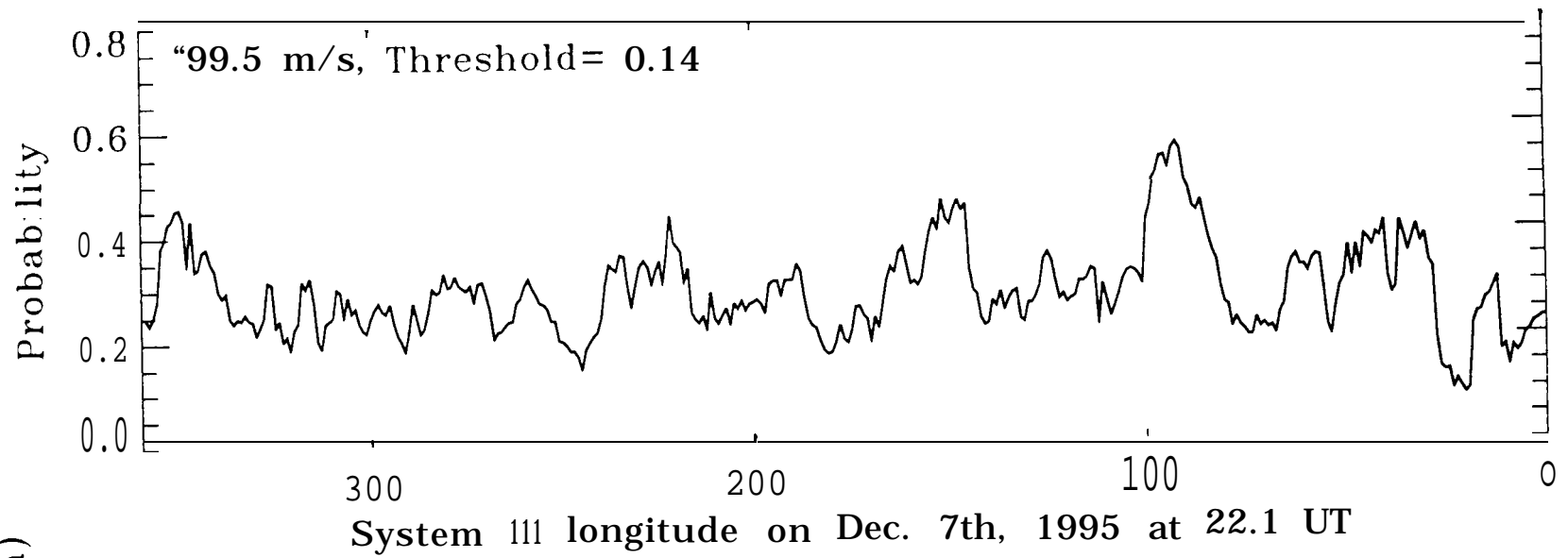


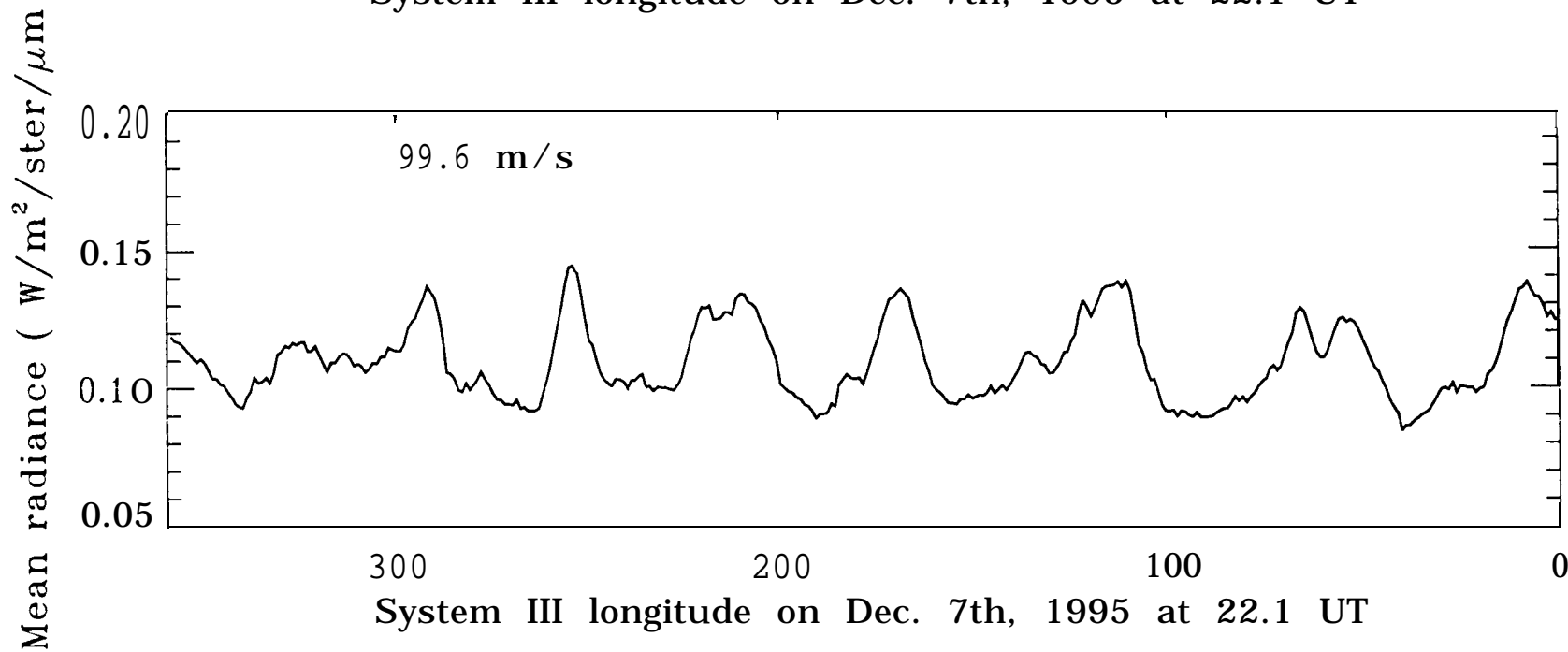
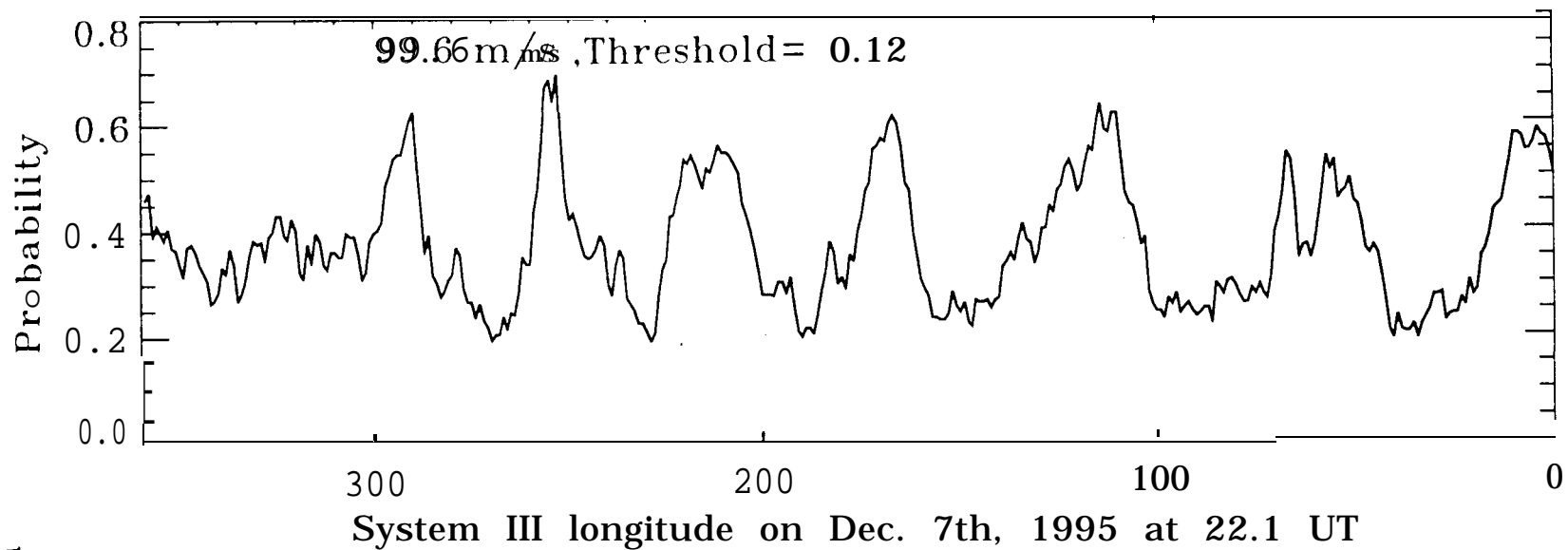


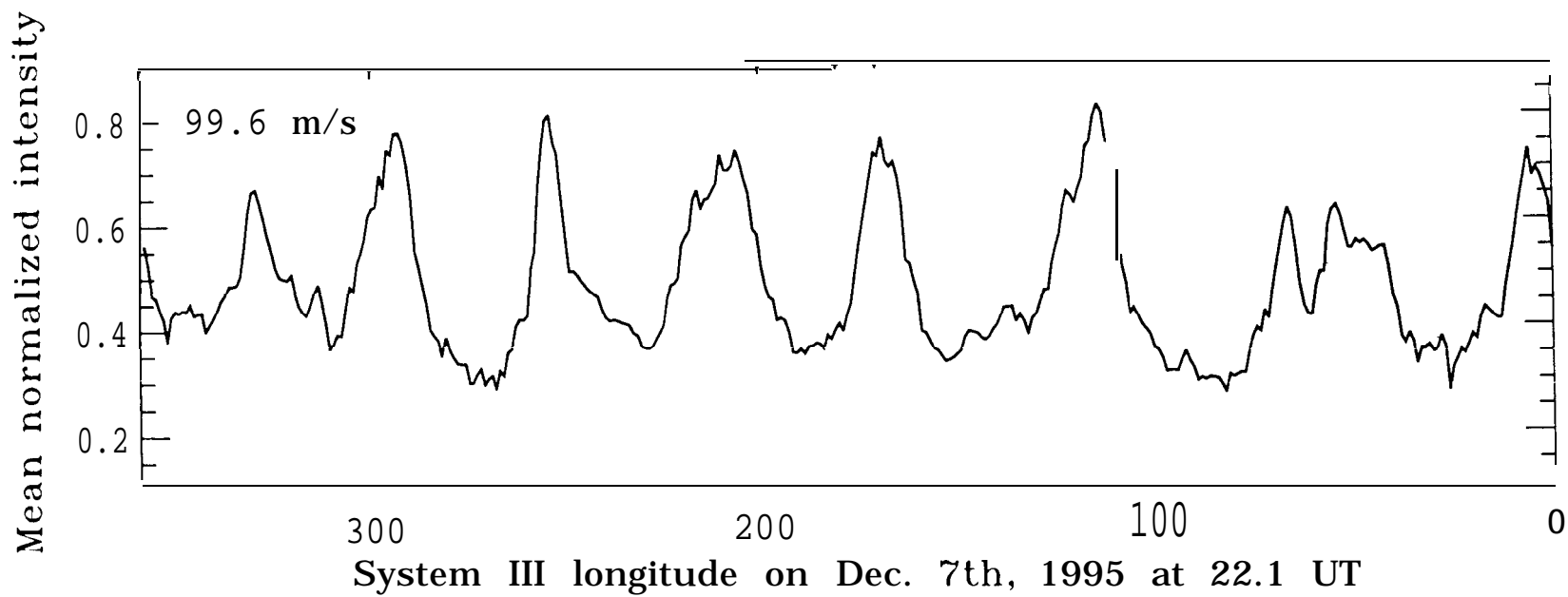
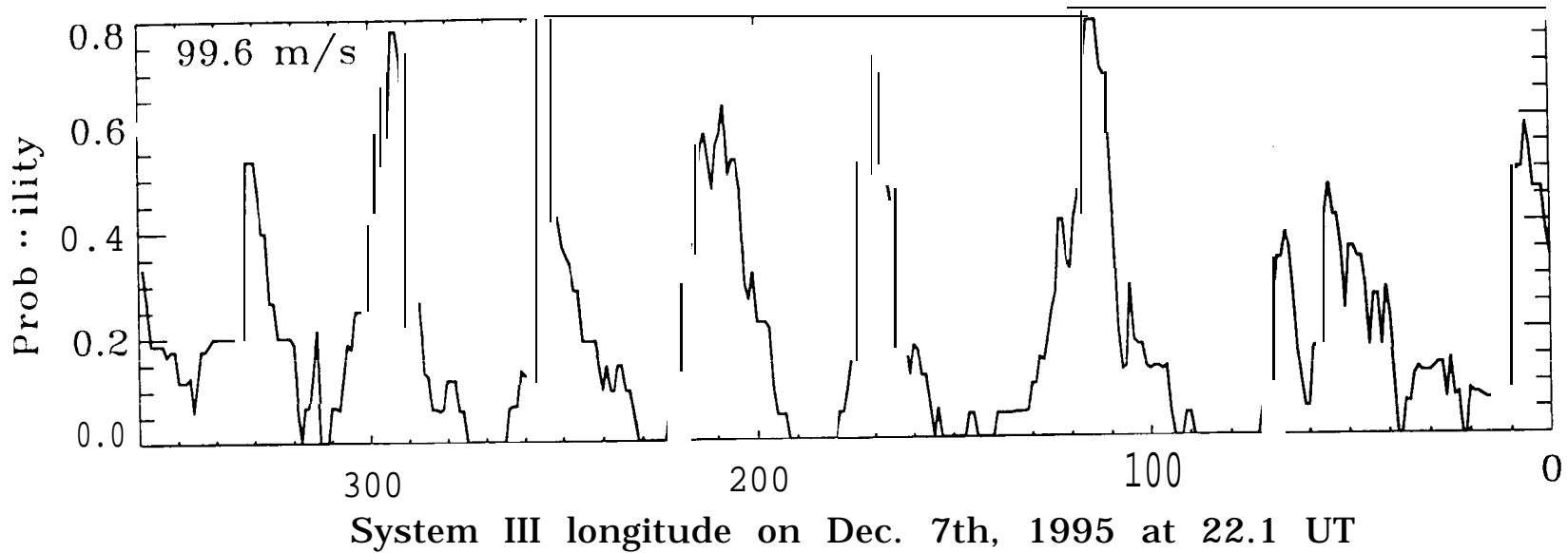
1995 Aug 9
1995 Aug 10
1995 Aug 11
1995 Sep 3
1995 Sep 4
1995 Sep 5
1995 Sep 6
1995 Sep 8
1995 Sep 16
1995 Sep 17
1995 Sep 18
1995 Sep 20
1995 Sep 26
1995 Sep 27
1995 Oct 2
1995 Oct 4
1995 Oct 5
1995 Oct 6
1995 Oct 13
1995 Oct 13
1995 Oct 14
1995 Oct 17

360 270 180 90 0
System III Longitude (°W)

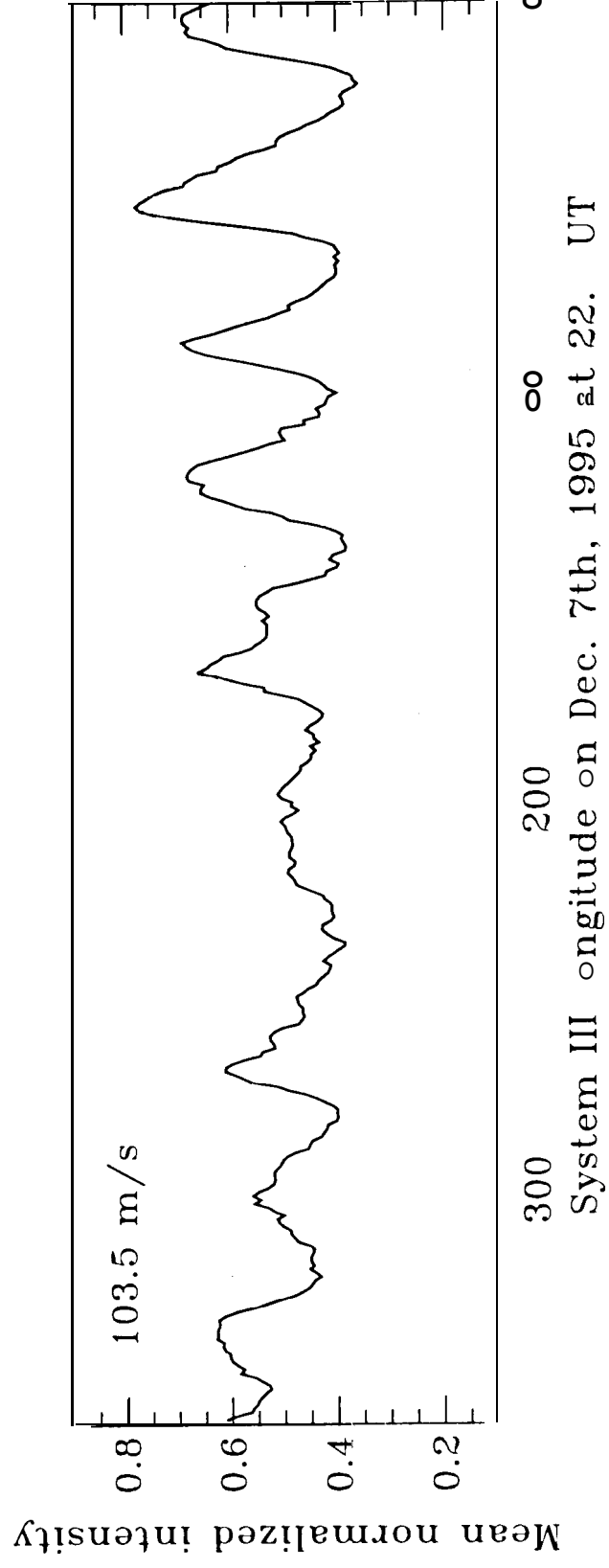
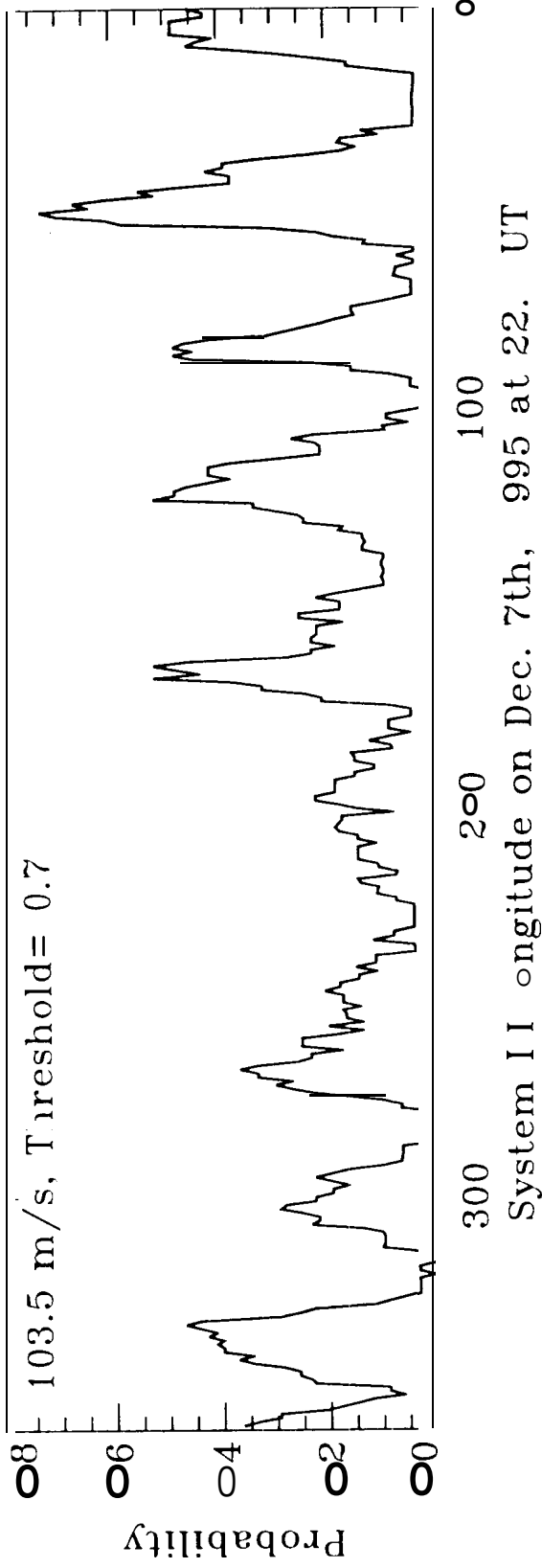


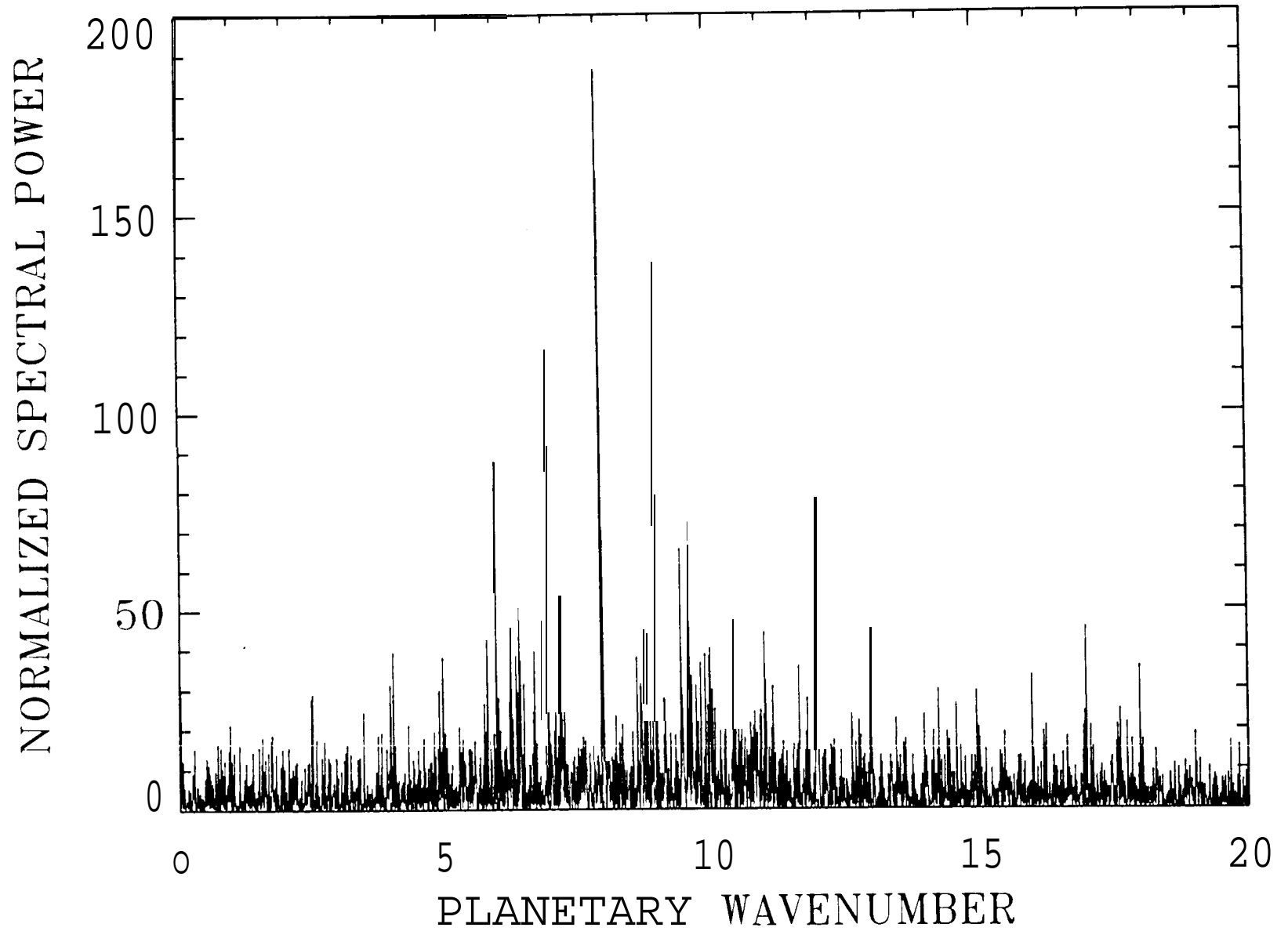


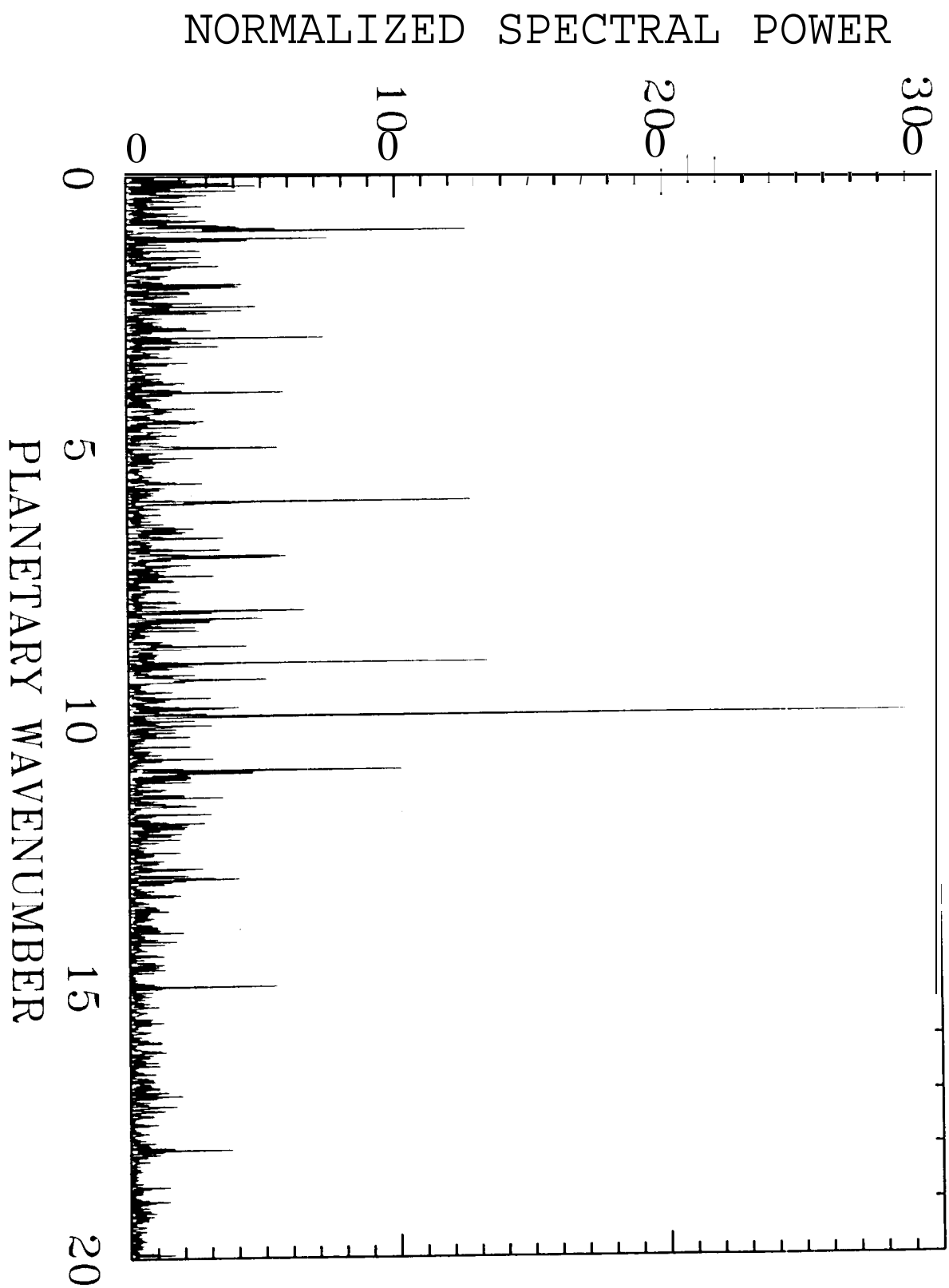


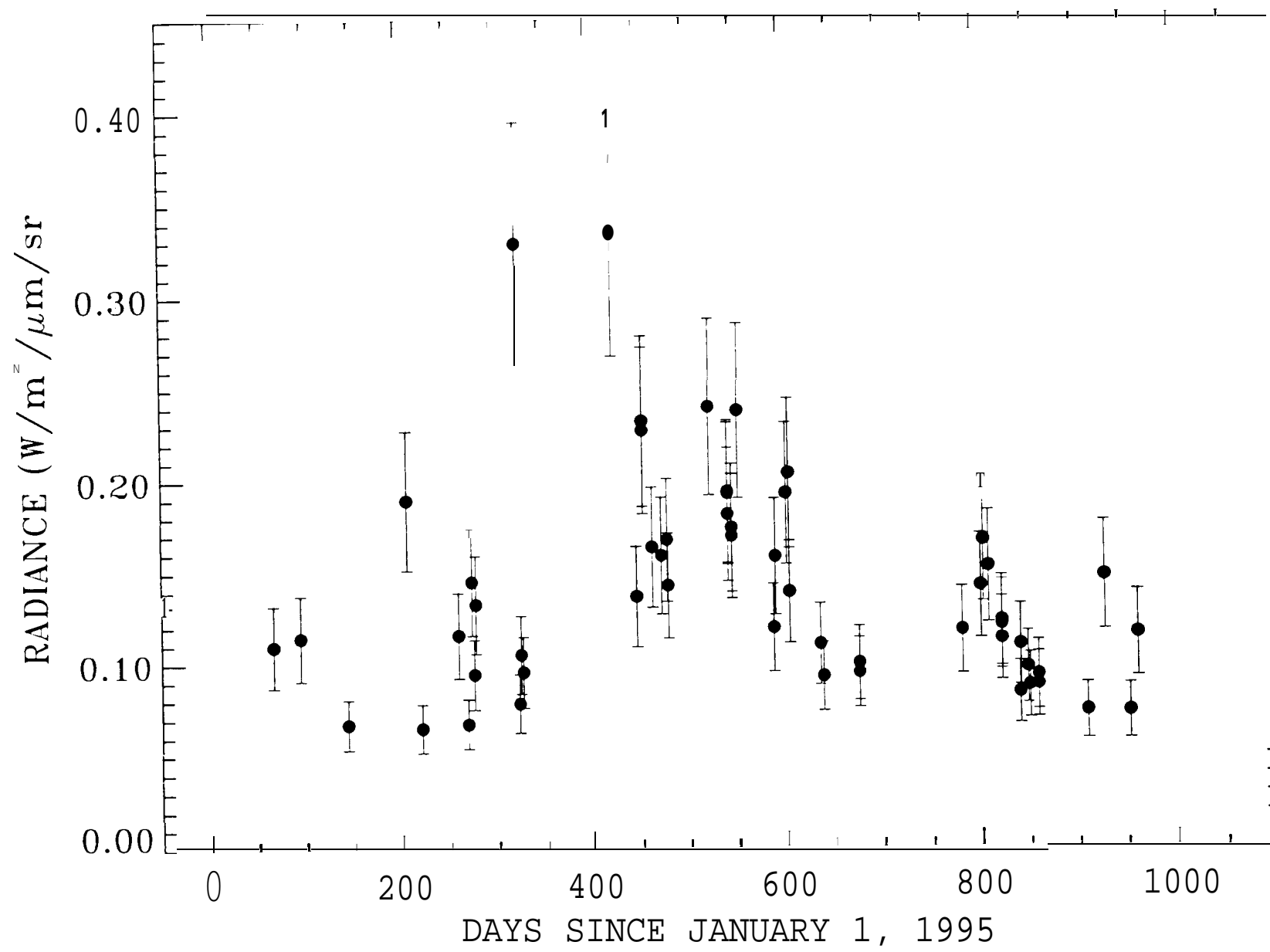


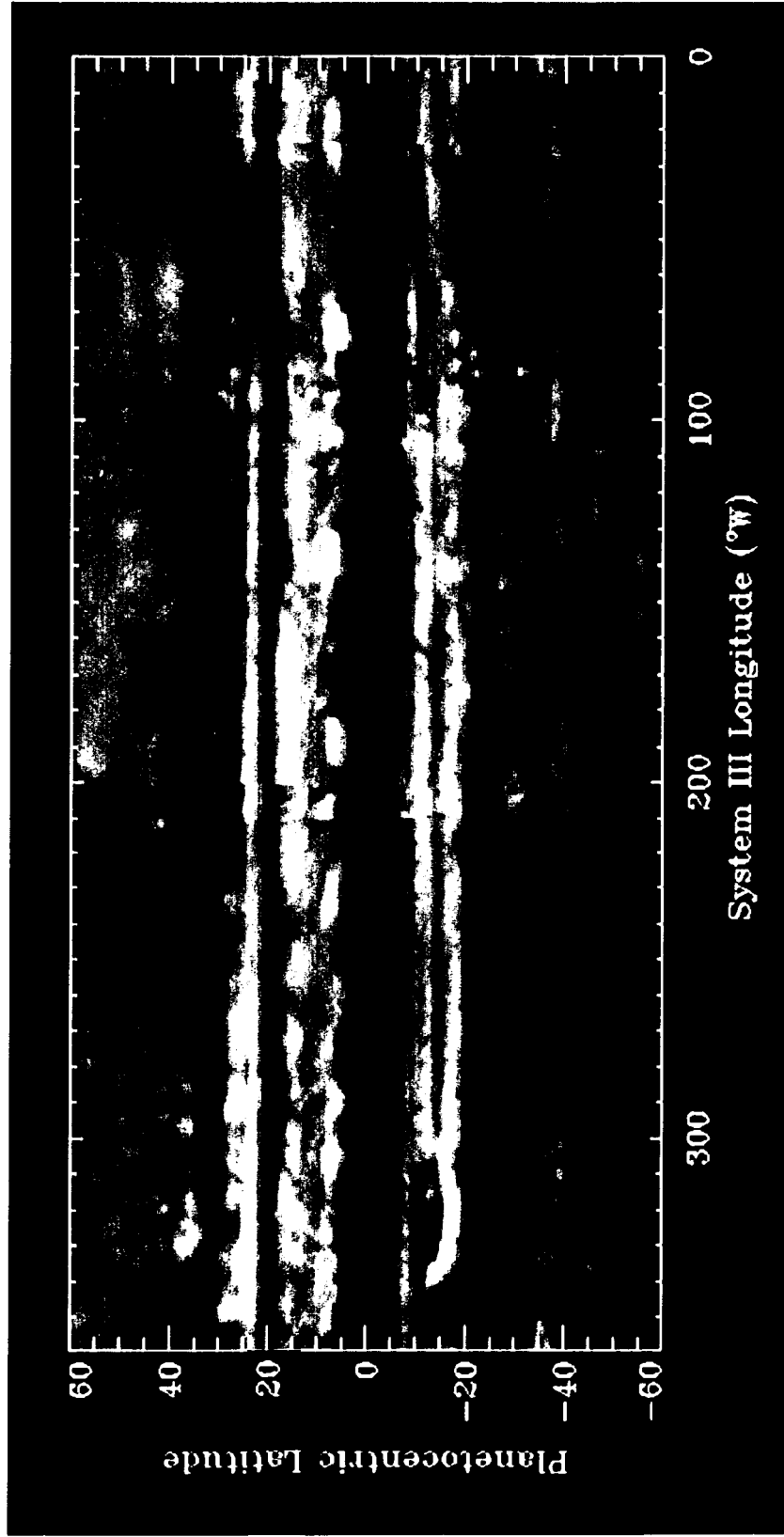
6B











DATE day/month/year)	INSTRUMENT	INSTRUMENT2	INSTRUMENT
29/12/93	NSFCAM		
30/12/93	NSFCAM		
06/01/94	NSFCAM		
25/04/94	NSFCAM		
28/04/94	NSFCAM		
12/07/94	NSFCAM		
17/07/94	NSFCAM		
19/07/94	NSFCAM		
27/07/94	NSFCAM		
28/07/94	NSFCAM		
03/08/94	NSFCAM		
07/08/94	NSFCAM		
19/02/95	NSFCAM		
27/02/95	NSFCAM		
01/03/95	NSFCAM		
02/03/95	NSFCAM		
08/03/95	NSFCAM		
09/03/95	NSFCAM		
10/03/95	NSFCAM		
11/03/95	NSFCAM		
14/03/95	NSFCAM		
05/04/95	NSFCAM		
15/04/95	NSFCAM		
20/05/95	NSFCAM		
23/05/95	NSFCAM		
24/05/93	NSFCAM		
11/07/95	NSFCAM		
26/07/95	NSFCAM		
27/07/95	NSFCAM		
09/08/95	NSFCAM		
10/08/95	NSFCAM		
11/08/95	NSFCAM		
03/09/95	NSFCAM		
04/09/95	NSFCAM		
05/09/95	NSFCAM		
06/09/95	NSFCAM		
08/09/95	NSFCAM		

Table I

DATE day/month/year)	INSTRUMENT1	INSTRUMENT2	INSTRUMENT3
16/09/95	NSFCAM		
17/09/95	NSFCAM		
18/09/95	NSFCAM		
20/09/95	NSFCAM		
26/09/95	NSFCAM		
27/09/95	NSFCAM		
02/10/95	NSFCAM		
04/10/95	NSFCAM		
05/10/95	NSFCAM		
06/10/95	NSFCAM		
13/10/95	NSFCAM		
14/10/95	NSFCAM		
17/10/95	NSFCAM		
06/11/95	NSFCAM		
07/11/95	NSFCAM		
18/11/95	NSFCAM		
19/11/95	NSFCAM		
20/11/95	NSFCAM		
21/11/95	NSFCAM		
22/11/95	NSFCAM		
24/11/95	NSFCAM		
07/12/95		MIRAC2	
22/01/96	NSFCAM		
23/01/96	NSFCAM		
23/01/96	NSFCAM		
13/02/96	NSFCAM		
29/02/96	NSFCAM		
02/03/96	NSFCAM		
23/03/96	NSFCAM		
30/03/96	NSFCAM		
31/03/96	NSFCAM		
08/04/96	NSFCAM		
18/04/96	NSFCAM		
19/04/96	NSFCAM		
24/04/96	NSFCAM		
24/04/96	NSFCAM		
25/04/96	NSFCAM		
26/04/96	NSFCAM		

Table I cont.

DATE day/month/year)	INSTRUMENT	INSTRUMENT2	INSTRUMENT3
' 11/05/96			CASPIR
29/05/96	NSFCAM		
30/05/96	NSFCAM		
31/05/96	NSFCAM		
01/06/96	NSFCAM		
02/06/96	NSFCAM		
03/06/96	NSFCAM		
04/06/96	NSFCAM		
05/06/96	NSFCAM		
07/06/96	NSFCAM		
26/06/96	NSFCAM		
27/06/96	NSFCAM		
28/06/96	NSFCAM		
29/06/96	NSFCAM		
30/06/96	NSFCAM		
02/07/96	NSFCAM		
03/07/96	NSFCAM		
04/07/96	NSFCAM		
07/07/96	NSFCAM		
08/07/96	NSFCAM		
09/07/96	NSFCAM		
11/07/96	NSFCAM		
12/07/96	NSFCAM		
11/08/96	NSFCAM		
12/08/96	NSFCAM		
13/08/96	NSFCAM		
14/08/96	NSFCAM		
20/08/96	NSFCAM		
21/08/96	NSFCAM		
23/08/96	NSFCAM		
24/08/96	NSFCAM		
25/08/96	NSFCAM		
26/08/96	NSFCAM		
27/08/96	NSFCAM		
28/08/96	NSFCAM		
29/08/96	NSFCAM		
01/09/96	NSFCAM		
28/09/96	NSFCAM		
29/09/96	NSFCAM		
30/09/96	NSFCAM		

Table I cont

DATE (day/month/year)	INSTRUMENT1	INSTRUMENT2	INSTRUMENT
02/10/96	NSFCAM		
03/10/96	NSFCAM		
04/10/96	NSFCAM		
22/10/96	NSFCAM		
26/10/96	NSFCAM		
28/10/96	NSFCAM		
06/11/96	NSFCAM		
07/11/96	NSFCAM		
08/11/96	NSFCAM		
09/11/96	NSFCAM		
10/11/96	NSFCAM		
11/11/96	NSFCAM		
20/11/96	NSFCAM		
30/11/96	NSFCAM		
06/12/96	NSFCAM		
17/12/96	NSFCAM		
18/12/96	NSFCAM		
19/12/96	NSFCAM		
20/12/96	NSFCAM		
21/12/96	NSFCAM		
19/02/97	NSFCAM		
20/02/97	NSFCAM		
21/02/97	NSFCAM		
22/02/97	NSFCAM		
12/03/97	NSFCAM		
14/03/97	NSFCAM		
15/03/97	NSFCAM		
19/03/97	NSFCAM		
20/03/97	NSFCAM		
21/03/97	NSFCAM		
30/03/97	NSFCAM		
31/03/97	NSFCAM		
02/04/97	NSFCAM		
03/04/97	NSFCAM		
05/04/97	NSFCAM		
19/04/97	NSFCAM		
20/04/97	NSFCAM		
21/04/97	NSFCAM		
25/04/97	NSFCAM		
26/04/97	NSFCAM		
27/04/97	NSFCAM		

Table I cont.

Table II. Evolution of the spectral power as a function of time and drift speed correction.

DATES USED	Speed (m/s)	Spectral power N=6	Spectral power N=7	Spectral power N=8	Spectral power N=9	Spectral power N=10	Number of maps
Feb 95- Aug 95	99.5	-			55	-	26
	100.5	-			80	-	26
	101.5	-			110	-	26
	102.5	-			125	-	26
	103.5	-			120	-	26
Apr 95- Ott 95	99.5	-			-	70	24
	100.5	-			-	85	24
	101.5	-			-	105	24
	102.5	-			-	100	24
	103.5	-			-	95	24
Jun 95- Dec 95	99.5	-		120	-	180	42
	100.5	-		125	-	190	42
	101.5	-		125	-	210	42
	102.5	-		120	-	225	42
	103.5	-		120	-	220	42
Aug 95- Feb 96	99.5	-		115	-	220	41
	100.5	-		125	-	235	41
	101.5	-		125	-	230	41
	102.5	-		120	-	230	41
	103.5	-		120	-	205	41
Ott 95- Apr 96	99.5	-		210	-	100	36
	100.5	-		230	-	140	36
	101.5	-		245	-	170	36
	102.5	-		235	-	190	36
	103.5	-		210	-	180	36
Dec 95- Jun 96	99.5	-		295	100	-	32
	100.5	-		295	100	-	32
	101.5	-		3 1 0	110	-	32
	102.5	-		290	120	-	32
	103.5	-		270	120	-	32
Feb 96- Aug 96	99.5	-		280	200	-	65
	100.5	-		290	200	-	65
	101.5	-		300	190	-	65
	102.5	-		290	170	-	65
	103.5	-		280	140	-	65
Apr 96- Ott 96	99.5	-	210	185	270	130	108
	100.5	-	200	195	260	145	108
	101.5	-	185	200	250	150	108
	102.5	-	170	200	235	170	108
	103.5	-	160	195	200	180	108

DATE (day/month/year)	INSTRUMENT1	INSTRUMENT2	INSTRUMENT3
28/04/97	NSFCAM		
29/04/97	NSFCAM		
30/04/97	NSFCAM		
01/05/97	NSFCAM		
06/05/97	NSFCAM		
07/05/97	NSFCAM		
08/05/97	NSFCAM		
09/05/97			CASPIR
10/05/97	NSFCAM		
13/05/97			CASPIR
19/05/97			CASPIR
21/05/97			CASPIR
23/05/97			CASPIR
24/05/97			CASPIR
25/05/97			CASPIR
30/05/97			CASPIR
31/05/97			CASPIR
01/06/97			CASPIR
05/06/97			CASPIR
06/06/97			CASPIR
07/06/97			CASPIR
08/06/97			CASPIR
09/06/97			CASPIR
10/06/97			CASPIR
11/06/97			CASPIR
15/06/97			CASPIR
16/06/97			CASPIR
17/06/97			CASPIR
18/06/97			CASPIR
19/06/97			CASPIR
20/06/97			CASPIR
22/06/97			CASPIR
23/06/97			CASPIR
27/06/97	NSFCAM		
29/06/97	NSFCAM		
30/06/97	NSFCAM		
06/07/97	NSFCAM		
17/07/97	NSFCAM		
18/07/97	NSFCAM		

Table I cont.

Table II. Continuation.

DATES USED	Speed (m/s)	Spectral power N=6	Spectral power N=7	Spectral power N=8	Spectral power N=9	Spectral power N=10	Number of maps
Jun 96- Dec 96	99.5	280	210	130	270	260	114
	100.5	270	200	120	255	270	114
	101.5	245	205	130	235	270	114
	102.5	235	210	140	210	260	114
	103.5	235	210	140	180	250	114
Aug 96- Feb 97	99.5	-	130	110	200	355	91
	100.5	-	120	115	195	340	91
	101.5	-	110	115	185	315	91
	102.5	-	100	120	170	300	91
	103.5	-	100	120	140	250	91
Ott 96- Apr 97	99.5	-	-	130	175	210	59
	100.5	-	-	125	175	235	59
	101.5	-	-	125	175	250	59
	102.5	-	-	125	160	260	59
	103.5	-	-	120	140	250	59
Dec 96- Jun 97	99.5	-	-	670	100	100	82
	100.5	-	-	660	100	100	82
	101.5	-	-	640	100	100	82
	102.5	-	-	600	100	100	82
	103.5	-	-	550	100	100	82
Feb 97 - Aug 97	99.5	-	100	910	90	-	96
	100.5	-	100	900	90	-	96
	101.5	-	100	850	100	-	96
	102.5	-	100	870	90	-	96
	103.5	-	100	840	90	-	96